Study of the pit initiation mechanism and metal dissolution kinetics during anodic etching of aluminum

by

Kamal Kumar Muthukrishnan

A thesis submitted to the graduate faculty

in partial fulfillment of the requirements for the degree of

MASTER OF SCIENCE

Major: Chemical Engineering

Program of Study Committee:
Kurt R. Hebert (Major Professor)
Rodney O. Fox
Vikram L. Dalal

Iowa State University

Ames, Iowa

2003

Graduate College
Iowa State University

This is to certify that the master's thesis of

Kamal Kumar Muthukrishnan

has met the thesis requirements of Iowa State University

Signatures have been redacted for privacy

TABLE OF CONTENTS

LIST OF FIGURES

LIST OF TABLES

ABSTRACT

The role of subsurface nano-scale voids present near the metal-oxide film interface, on pit nucleation was investigated. Electrochemical processes during the initial stages of etching were thoroughly characterized to evaluate the hypothesis that voids are the primary pit initiation sites. Dissolution rate measurements made in etch pits revealed contradicting trends of constant and potential dependent dissolution current densities. The same trends were also exhibited by the measurements made in etch tunnels, which eliminated the possible role of geometric form of corrosion in such a contradiction. Finally it was concluded that the experimental time-scale during which the dissolution rate measurements were made, was the only factor responsible for such varying trends. A kinetic model similar to the Vetter-Gorn model for metals covered with oxide films was proposed. The model was validated by its ability to predict the observed constant and potential dependent dissolution rates under different experimental-time scales.

A mathematical model for pit initiation during the initial stages of galvanostatic anodic etching of aluminum in acid-chloride solutions was developed. The model incorporated all of the electrochemical processes characterized during the initial stages of etching and was based on the interfacial void hypothesis which assumes voids to be the only pit initiation sites. The effect of various experimental conditions such as caustic pretreatment time, applied current density, etchant temperature, chloride concentration in etchant etc. were analyzed using the etching potential transient. The dependence of void concentration on the caustic pretreatment time was determined by fitting the potential transients and the observed trend had a fine agreement with previously established PAS results. Using the fit void concentrations, the model could successfully track the experimental transients for various

etchant temperatures and applied current densities. However, the model failed to predict the temperature-dependent pit depths found experimentally, which might be due to the simplified assumptions made in its development. Also the role of chloride ion kinetics in pit initiation mechanism should be clearly understood and incorporated in the model for successfully predicting the experimental results obtained for varied chloride concentrations in the etchant.

1. INTRODUCTION

Electrolytic etching is a process by which the aluminum foils are anodically polarized, to produce localized corrosion attack and thus achieve high surface area. Capacitors made from these foils have a very high capacitance gain due to the increased surface area. Hence, this serves as the standard fabrication process in the electrolytic capacitor industries.

Etching generates pits with active dissolving surfaces. Figure 1.1 shows a Scanning Electron Microscope (SEM) image of hemispherical pits developed after etching the foil for 75 ms at 70 ^{0}C and 200 mA/cm^2. These pits which are prominent only during the very early stage of etching, get transformed immediately to cubic etch pits, which later develop into elongated structures called etch tunnels at prolonged times of etching.

Using positron annihilation spectroscopy (PAS), Wu et al. discovered numerous voids located near the metal oxide film interface, and also found that their metallic surface was oxide-free (1). He also found that voids are also produced by caustic pretreatment. Atomic Force Microscope (AFM) images of pretreated foils, revealed cavities when the surface oxide film had been chemically stripped. Based on quantitative agreement of cavity depth and coverage with the PAS results, it was suggested that cavities are the interfacial voids exposed by stripping. The pit size distribution on etched foil surface was found to be similar to that of cavities, suggesting that interfacial voids may be the primary pit initiation sites.

The main purpose of this work is to examine in detail, the etching behavior of aluminum foils, based on the electrochemical measurements, during the initial stages of

etching. A mathematical model for these measurements is developed to test the hypothesis that pits nucleate from interfacial voids.

The entire work can be divided into three parts. In the first part electrochemical processes during the first 100 ms of etching were thoroughly characterized to obtain kinetics of metal dissolution and oxidation process during these times. Al foils were etched in 1M HCl and 3M H_2SO_4 at 70 °C for various times and were examined by SEM to reveal pit size distributions. Experiments were also done in 3M H_2SO_4 wherein oxidation is the only dominant process; this helped to characterize the oxidation kinetics during etching. The applied current was rapidly decreased through a series of steps and the corresponding transients were obtained. Based on the current-potential dependence during this sequence it was possible to elucidate kinetics of metal dissolution and anodic oxidation.

In the second part, further information on pit dissolution kinetics was found, using the pitting current and pit surface area from SEM. Also, the dissolution kinetics in etch tunnels was investigated by the current pulse technique introduced earlier by Tak et al. (2). The results revealed potential dependent dissolution rates. A kinetic model for metal dissolution in pits, similar to the Vetter-Gorn model for metals covered with oxide films (3, 4), was proposed. The model predicts potential-dependent and independent dissolution rates, depending on the time scale of their measurements.

In the third and final part of the work, the various electrochemical processes characterized during the initial stages of etching were incorporated into a mathematical model, which assumes voids to be the only pit precursor sites. The validity of the model was tested by its ability to predict the experimental transients for various pretreatment times and etching conditions.

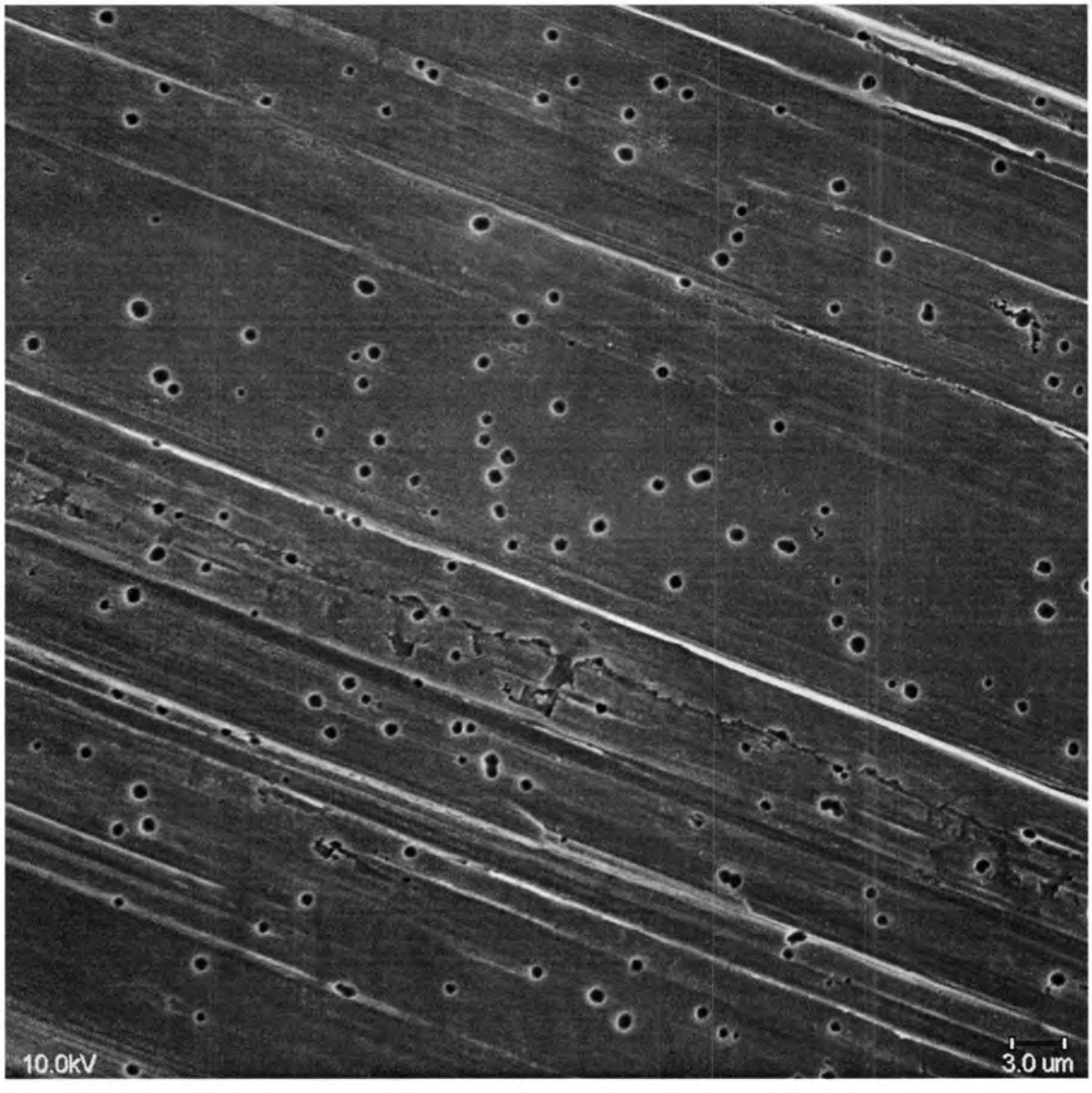

Figure 1.1 SEM image showing hemispherical pits developed by galvanostatic etching of aluminum. Etching current density 200 mA/cm^2, temperature 70 ^{o}C, etching time 75 ms and NaOH pretreatment time 30 s.

2. LITERATURE REVIEW

The first section in this chapter deals with the various mechanisms that have been proposed for nucleation of pits. Since the present work is based on the hypothesis that voids are the primary pit initiation sites, the second and the third sections mostly discuss the mechanisms of void formation, and some of the evidences that portray voids to be the pit precursor sites. As already explained in the introduction, one of the main objectives of the present work is to characterize the various electrochemical processes during the initial stages of etching. With regard to this, the fourth section focuses on previous work on the early stages of etching. The interfacial void hypothesis and earlier studies on pit dissolution kinetics are discussed in the concluding sections.

2.1.Various Mechanisms for Pit Formation

Many researchers have studied pitting corrosion by experimental techniques. Over the past decades, several mechanisms for pit formation have been proposed. H. H. Strehblow (5) categorized the pit initiation theories into three main mechanisms that emphasized passive film penetration, film breakdown, and adsorption of aggressive anions.

2.1.1. Penetration through passive film

Passive films are inert oxide films formed over the surface of bare metals, thus decreasing their susceptibility to corrosion in aggressive environments. They are usually 5-10 nm in thickness and can support extremely high electric field (~ 10^6-10^7 V/cm).

Hoar et al. (6) described the penetration mechanism of aggressive anions through the passive oxide films. According to their theory, the electrostatic field across the film/solution

interface influences these anions to penetrate the oxide film at singular points. These sites may be grain-boundary, grain-margin, or disordered zones, or regions of elevated impurity concentrations in the metal (5). When the concentration of anions in the oxide film reach a critical value, the film breaks down and pits initiate immediately.

H.H. Strehblow (5) suggested that the anions adsorb at preferential sites on the surface of oxide layer, which are energetically favorable for adsorption. In the process, they replace OH^- or O^{2-} ions of the passive oxide to maintain electrical neutrality and thus penetrate into the film. This oxide layer incorporated with aggressive anions has a greater dissolution velocity than the normal oxide. This leads to its partial or complete removal at these preferential adsorption sites. Also, the metal dissolution is enhanced locally at these sites due to the increased field strength existing across the relatively thin passive layer.

Bessone et al. (7) interpreted the adsorption and penetration of aggressive anions in surface oxide films by analyzing the impedance spectra obtained at low frequencies and at potentials close to pit initiation. Kruger et al. (8), through their ellipsometric work, strongly supported the ion penetration theory. According to this theory the Cl^- ions are incorporated into the passive film and then migrate to the metal-film interface to promote film breakdown. Later, contradictory results comparing the penetration of Cl^- ions and the onset or induction time for pitting were found (5).

2.1.2. Adsorption of aggressive anions

The first adsorption mechanism for pit initiation was proposed by Uhlig (9). According to him, the anions displace the adsorbed passivators like oxygen or chromates and get adsorbed at those sites. They immediately start reacting with the metal since the

activation energy for their reaction is low compared to that of oxygen and chromates, and thus pitting initiates. Later it was found that the passive film was several monolayers thick, contradictory to a single adsorbed oxygen layer as assumed in the above theory.

Uhlig (10, 11) and Kolotyrkin (12) proposed that, above a critical potential called the breakdown potential, Cl^- adsorption is favored over O^{2-} adsorption in the passive layer. The adsorbed Cl^- anions hinder passivation and promote film breakdown.

2.1.3. Breaking of the passive oxide layer

Strehblow gave a generalized theory that breaking of the passive layer would favor the direct contact of the bare metal surface with aggressive anions leading to pit initiation. Though he mentioned the mechanical stresses and surface tension due to adsorption on the passive layer as factors favoring breakdown, a detailed mechanism was not proposed.

Mechanical flaws were also thought to be significant factors in the film breakdown mechanism. In one of his earlier studies Hoar (13, 14) assumed that mechanical stresses develop in the thin air-formed oxide film on metal, when it comes in contact with aggressive electrolytes and lead to the formation of pores and flaws. Richardson and Wood (15) attributed local breakdown events to mechanical stresses at weak sites or flaws. Sato (16) proposed that the adsorption of anions reduces the surface tension and increases the pressure in the passive films. According to him, when this pressure exceeds a critical value, the film breaks down. Hoar (17) suggested that, when the repulsive force between the adsorbed anions is sufficiently high, the film tends to crack.

2.1.4. Other mechanisms

2.1.4.1. Dissolution mechanism

Hoar and Jacob (18) suggested that the cations readily form high-energy complexes with Cl^- anions on the surface of the passive film, and the entire complex immediately dissolves into the solution. Thus the film becomes thinner locally due to which the electric field strength and the metal dissolution are enhanced. The process gets repeated when more cations are readily transported to the surface, finally resulting in "auto-accelerated" breakdown. Foroulis and Thubrikar (19) proposed a similar mechanism according to which the chloride ions form soluble, basic chloride salt with the metal cations. The corresponding reactions are as given below:

$$Al(OH)_3 \leftrightarrow Al(OH)_2^+ + OH^- \tag{2.1}$$

$$Al(OH)_2^+ + Cl^- \rightarrow Al(OH)_2 Cl \tag{2.2}$$

2.1.4.2. Local acidification mechanism

The local acidification theory for pit formation was first suggested by Hoar in 1937 (20) and later developed by Galvele (21, 22) in 1976. According to them, metal ions hydrolyze inside the micropits already existing on the surface of the metals, leading to local acidification, which prevents repassivation. The hydrolysis reaction is given by (23),

$$Me^{z+} + zH_2O = Me(OH)_z + zH^+ \tag{2.3}$$

2.1.4.3. Alloying effects

Many researchers have discussed alloying effects on pit initiation. The effect of MnS inclusions on the localized corrosion of stainless steel was explained by Eklund (24) and Wranglen (25). According to Eklund, the sulfide inclusions, which are good electronic conductors, become thermodynamically unstable and tend to dissolve when polarized to relatively high potentials. Thus they expose the bare metal surface to the corrosive environment. Using in situ atomic force microscopy, Rynders et al. (26) monitored the enhanced localized corrosion near iron rich inclusions in aluminum alloys. These inclusions, which are very good oxygen reduction agents, increase the pH by local alkalization as suggested by Nisancioglu (27). They suggested that the local increase in pH at these inclusions degrades the passive film surrounding them, and promotes dissolution.

Using in situ corrosion studies, Kowal et al. (28) explained the effect of copper on the intergranular corrosion of aluminum alloys. The incomplete quenching of Al-Cu alloys leads to the formation of second phase precipitates and copper depleted regions in the vicinity of grain boundaries (29). Kowal et al. suggested that the faster dissolution rates at these Cu depleted regions leads to the intergranular corrosion.

2.1.4.4. Stabilization of metastable pits

Metastable pits are pits that can initiate at potentials well below the pitting potential, and also during the induction period where the potential is higher than the pitting potential. They initiate and grow for a limited period called the 'critical age' after which they get repassivated (30). Previous works by Williams et al. demonstrated the role of metastable pitting in pit initiation (30-32). Their stochastic model for pitting corrosion in stainless steel,

assumes that these metastable pits transform into active etch pits once they survive the critical age. However many of the metastable pits are repassivated before the critical age. In order to explore the process that triggers the formation of metastable pits, Zhu and Williams carried out sensitive current mapping measurements at low potentials, which revealed a few regions of relatively high passive current density (33). When stepped to a higher potential, exactly these regions developed into pits. This yielded a relationship between regions of high passive current densities and pit nucleation sites. According to the derivation given by Williams et al., the criterion for pit stabilization is that I_{pit}/r_{pit} must exceed a value of approximately 4×10^{-2} A/cm, where I_{pit} refers to the peak pit current and r_{pit} represents the pit radius (34). Pride et al. validated this stabilization criteria by anodically polarizing high purity aluminum wires in chloride solutions (35). The current spikes during pitting events obtained for different applied potentials were carefully analyzed and the peak pit currents were plotted against the pit radii at the peak current. It was observed that when the potential was increased, the ratio I_{pit}/r_{pit} gradually increased to the value 4×10^{-2} A/cm indicating the formation of stable pits.

Lack of quantitative analysis of the experimental data remained a major drawback for these models, although they were able to explain some trends qualitatively. Further none of the mechanisms described above explored the effect of pretreatment on the rate of pit initiation. The pretreatment is found to decisively influence pitting during anodic etching of aluminum.

2.2. Mechanism of Interfacial Void Formation

The point defect model developed by Macdonald and coworkers explained the formation of voids at the metal oxide interface (36, 37). The model states that the growth of passive films involves the diffusion of oxygen anions from the film-solution interface to the metal-film interface resulting in film thickening and the diffusion of metal cations from the metal-film interface to the film-solution interface resulting in dissolution. The diffusion of metal cations from the metal-film interface creates metal vacancies called the "metal holes" at the interface, which tend to submerge into the metal and disappear. But when the rate of formation of these vacancies is sufficiently higher than that of their submergence, they pile up and condense to form voids at the metal-film interface.

Voids are also formed after the annealing process in the manufacture of aluminum foils (38). Previously it was shown by Doherty and Davis (39, 40) that voids are formed at the metal oxide interface, when aluminum was annealed for an extended period at 640 ^{0}C and furnace cooled. They suggested that these voids were formed by the condensation of thermal vacancies. Hebert et al. (41) suggested a similar mechanism for the formation of interfacial voids after sodium hydroxide pretreatment. According to them, vacancies are generated at the metal-film interface due to the metal atom oxidation during dissolution in NaOH. At times after the NaOH treatment, these vacancies condense by solid state diffusion and generate voids.

Using Rutherford Backscattering Spectrometry and Auger Electron Spectroscopy Wu and Hebert (42) revealed that the near surface concentration of non-reactive metallic impurities like iron, copper and gallium build up continuously during dissolution of aluminum in NaOH. It was shown that the thickness of this impurity segregation layer was

approximately 10 nm. Previous work by Cigada and coworkers (43) also reveals surface enrichments of the metallic impurities in 99.98% aluminum subjected to alkaline etching.

Wu et al. observed significant concentrations of near-surface solid state defects such as vacancies and micro voids in aluminum pretreated in NaOH (1). The defect layer thickness was found to be ~100 nm in as-received foil and ~10 nm in pretreated foil. Since the thickness of the impurity segregation layer exactly matches with that of the defect layer thickness, it was suggested by Hebert et al. that impurities might play a possible role in the formation of voids near the metal-film interface (41).

2.3. Evidences for Voids as Pit Initiation Sites

One of the very early models that portray voids to be the pit initiation sites was suggested by Hoar et al. (6). According to the model, the vacancies at the metal-film interface that undermine the oxide film condense to form voids at the interface. The nucleation of void may cause the film to collapse and expose the underlying metal. A similar kind of mechanism was later proposed by Macdonald and coworkers in their Point Defect Model as explained in the previous section (36, 37). This model suggests that when the voids at the metal-film interface grow to a critical size, the film becomes thermodynamically unstable and collapses. This exposes the bare metal surface beneath it to the corrosive environment and leads to pit initiation. Most of the evidence for voids to be the pit precursor sites are given by Hebert and coworkers.

The first extensive use of positron annihilation spectroscopy in detecting atomic-scale near surface defects by Wu et al. (1), provided significant evidence that voids assist in pit nucleation. In order to characterize these defects, isochronal annealing was done up to 660 °C

and it was found that the defects did not anneal even at such high temperatures. It was concluded that these defects were impurity complexed voids or vacancy clusters, or interfacial voids at the metal-film interface located at microscopic surface roughness features. Arai et al. (44) and Diegle (45) previously had revealed the influence of near-surface impurities on the distribution of pitting sites. Also it was frequently observed that the surface roughness features were the most preferred locations for pit initiation. These results led the authors conclude that defects may serve as pit initiation sites.

Recent work by Hebert et al. (41) which compares positron measurement results with atomic force microscopy (AFM) images of aluminum foils after oxide film stripping, provides evidence for voids to be the primary pit nucleation sites. Using positron annihilation spectroscopy (PAS), the variation of defect layer S parameter (corresponding to the fraction of open-volume defects in the defect layer adjacent to the metal-film interface) with the NaOH pretreatment time was obtained. It was also found that the internal surface of the voids was oxide-free. AFM images obtained for pretreated foils, whose oxide film was stripped in Cr_2O_3-H_3PO_4 solution, revealed irregular cavities, which were 20 to 140 nm in depth. The number, distribution and shape of these cavities varied significantly with the pretreatment time. The variation of the cavity area coverage as revealed in the AFM images was nearly the same as that of the defect layer S parameter, which suggested that cavities form by dissolution of interfacial voids detected by PAS.

AFM images of etched aluminum foils revealed that the etch pits were mainly oriented along the surface ridges for the as-received foils and were more evenly distributed along the surface for pretreated foils (46). The same kind of distribution was observed for the cavities revealed after oxide film stripping. From the AFM images, it was also observed that

the cavity size was similar to those of pits observed after etching for a few milliseconds. Thus from the quantitative comparison of PAS detected defects with cavities revealed by AFM and from the qualitative comparison of cavity and pit morphology and distribution, it was concluded that pits nucleate from the interfacial voids.

2.4. Previous Studies on the Initial Stages of Etching

Characteristic potential transients during the early stages of galvanostatic etching in HCl solutions were reported by Wiersma and Hebert (47) and Osawa et al. (48) (Figure 2.1). The etching experiments were all done at elevated temperatures and for duration of less than 100 ms. It was observed that, at the instant the constant current pulse was given, there was almost a discontinuous jump in the potential followed by a gradual increase in potential to a maximum value. After attaining its peak the potential was found to fall abruptly to a very low value, which was close to the repassivation potential. This potential represents the potential of aluminum below which passivation occurs in pits. When the potential is maintained at this steady state value, the etch pits slowly are transformed into elongated structures called etch tunnels which are characterized by dissolution in direction normal to the metal surface. The continued process of etching is known as tunnel etching.

Wiersma (49) explained the effect of capacitive and metal dissolution current density on the shape of the potential transients. He found that anodic charging current contributes a significant part of the applied current during the very early stages of etching. Later, pits nucleate and the metal dissolution current density supplies a greater fraction of the applied current. When the potential reaches its maximum value, the metal dissolution supplies the entire applied current. He also found that, after the potential maximum, a

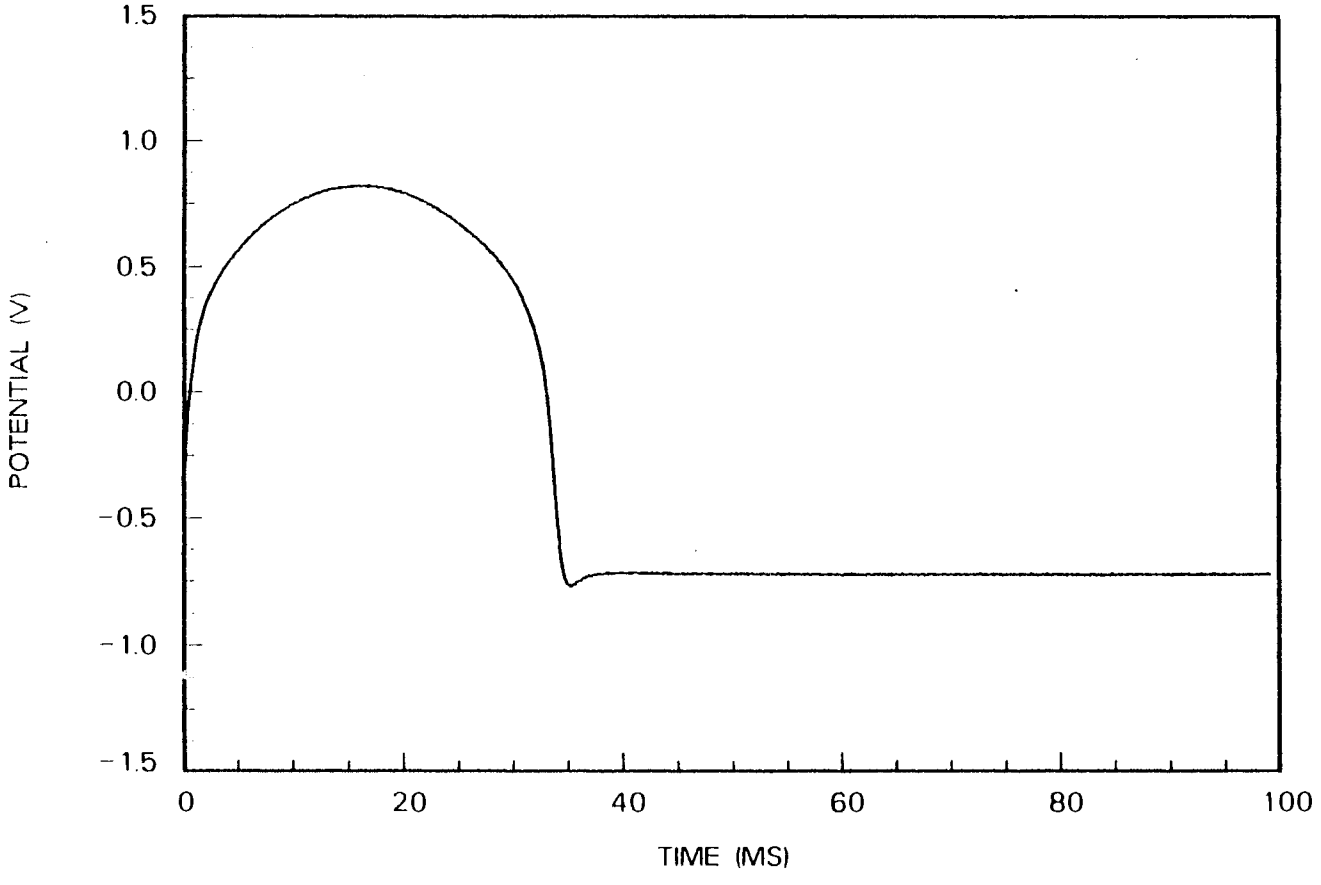

Figure 2.1 Potential transient during etching of as-received foil. Etchant 1M HCl, temperature 70 °C, applied current density 12.89 mA/cm^2.

Taken from B. J. Wiersma, Ph.D. Thesis, Iowa State University, Ames, IA (1990).

cathodic charging current must be present to maintain a constant applied current or otherwise the nucleation of new pits will indicate that the metal dissolution current density exceeds the applied current. The cathodic current density is reduced from a significant value to zero at the base of the transient, wherein the potential reaches its steady state value. It was suggested that part of the active area gets repassivated at such low potentials in order to maintain the constant applied current.

Similar transients were obtained by Flis and Kowalczyk (50) during the electrolytic etching of aluminum in NaCl solutions with and without Na_2SO_4. They found that both double layer charging and oxide growth influenced the initial rise in potential. According to them, only at the potential peak, the oxide film breaks down and pits start to nucleate. The steady state potential after the peak denotes the steady growth of pits and tunnels and it is represented as the pit growth potential E_{pg}.

The effects of parameters like NaOH pretreatment time, applied current density and etching temperature on the initial stages of etch pit development were studied by Wiersma (48). He found that the pit sizes did not increase significantly with increase in applied current density, but the pit density increased by a factor of 10. It was also observed that when the etching temperature increased, the mean square pit depth decreased, and the overall pit density increased. Martin and Hebert (46) observed that the time elapsed during the potential peak obtained during the initial stages of etching is inversely related to the pit nucleation rate. Using ex situ AFM images taken at various etching times during the early stages of the process, they suggested that the nucleation of new pits is significantly faster during the potential peak, compared to the later times.

Using scanning electron micrographs of resin replicas, Osawa and Fukuoka (51) studied the pit nucleation behavior of aluminum foils during the early stages of etching. They concluded that the pits that first nucleate during the initial high potential period have a hemispherical structure. Later the crystallographic dissolution of the (100) faces is favored, and they transform to half-cubic pits. Using transmission electron micrographs, they showed that pits with facets grow at the steady state potential, which is regarded as the pitting potential.

2.5. Dissolution Kinetics from Current Pulse Experiments

The study of dissolution kinetics of etch pits are of much importance in understanding the basic relation between the surface condition of the metal inside the pit and the mechanism of metal dissolution. Based on the potential dependence of the dissolution current density, Hunkeler and Bohini (52, 53) concluded that the dissolution rate of aluminum is controlled by the ohmic resistance of the solution inside the pit. But for very high potentials, a current plateau was observed by Frankel and co-workers for two-dimensional pits in thin aluminum films (54, 55) and this region was ascribed to mass-transport limited dissolution. In his study on artificial pits in concentrated $AlCl_3$, Beck found two distinct regions corresponding to ohmic and mass transport controlled corrosion rates (56). But in the case of very small etch pits and highly conductive etchant solutions, it was thought that exceedingly high current densities would immediately induce salt film precipitation on the metal surface (57) and the ohmic resistance of the solution becomes negligible. Thus pit dissolution would be controlled by mass transport at all potentials, as suggested by Wong and Alkire (58) and Buzza and

Alkire (59). Thus a thorough knowledge of dissolution kinetics plays a vital role in predicting the conditions required for the ohmic and mass-transport control of corrosion rates.

Many authors have reported a constant dissolution rate for steady state tunnel growth in 1N HCl etchant at 65 ^{0}C (60-62). It was observed by Wiersma and Hebert (47) and Lin and Hebert (63) that in contrast to this constant dissolution rates in etch tunnels, the dissolution current density in etch pits can be as high as 20 - 30 A/cm^2, when they nucleate, after which it falls to the constant value obtained for etch tunnels. Such high dissolution rates, which are potential dependent, are also observed for tunnel etching when anodic pulses were given during their growth, as explained in the following sections. The present work describes a kinetic model, which explains the apparent contradiction exhibited by the time scale dependent dissolution kinetics.

2.6. The Interfacial Void Hypothesis

Using Positron Annihilation Spectroscopy (PAS), it was previously found that voids are formed near the metal oxide interface when aluminum is pretreated in sodium hydroxide solution (1). Also, voids are apparently formed during the annealing process in the manufacture of aluminum foils. These voids are distributed over a thin layer in the metal close to the metal oxide interface, called the defect layer. According to this hypothesis, interfacial voids develop into etch pits when exposed to the etchant solution. The process can be represented schematically as shown in Figure 2.2. The uniform corrosion processes at the metal/oxide film interface move this interface deeper into the metal, represented as vertical downward arrows in Figure 2.2. Also, the oxide/solution interface moves in the same direction as of the metal/oxide interface, as metal ions are dissolved in the etchant solution.

When the metal/oxide interface comes in contact with the voids, the pressure difference across the oxide film makes it collapse, as shown in the following diagram.

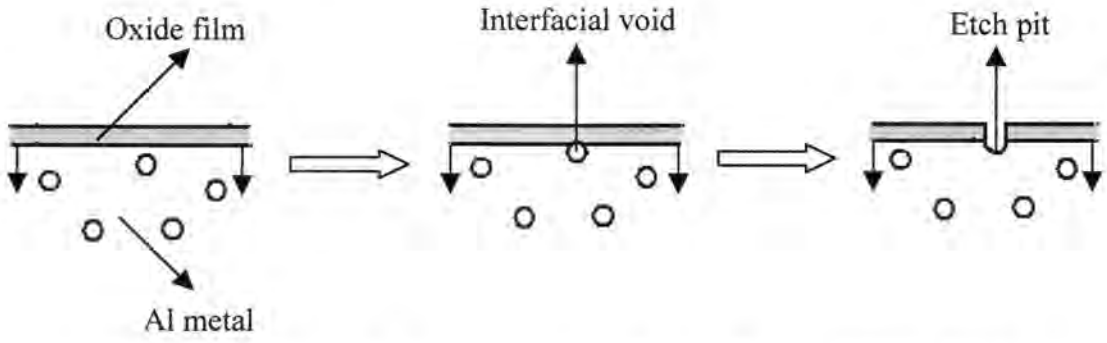

Figure 2.2 Schematic representation of the interfacial void hypothesis

Once the oxide film exposes the bare metal surface present inside the void to the aggressive etching solution, active dissolution begins and the voids are transformed to etch pits.

3. EXPERIMENTAL

3.1. Etching Apparatus and Set-up

The electrochemical cell for etching was a 300 ml beaker containing the acid etchant, a glass electrode area of known exposed area, a reference electrode, and a counter electrode. Figure 3.1 shows the schematic diagram for the glass electrode holder with the counter electrode, similar to the one used by Alwitt et al. (60). The working electrode (anode) was clamped between the two glass plates, exposing 5 cm^2 of its surface area to the etchant. A platinum counter electrode was fixed in a semicircular loop fashion above the anode to provide uniform current distribution over the entire exposed area.

The current during etching was supplied by a Potentiostat / Galvanostat (EG&G PAR 273). A GPIB-PCII (National Instruments Co.) interface between the personal computer (Pentium) and the galvanostat was used to apply the programmed current waveforms during etching. The output potential transients were measured by a High Speed Voltmeter at a sampling rate of 10-60 μs with a resolution of 1 mV. The readings were transferred to the computer using the GPIB-PCII interface. Figure 3.2 shows the entire experimental set-up for applying current waveforms to the etching cell and obtaining potential transients from the voltmeter.

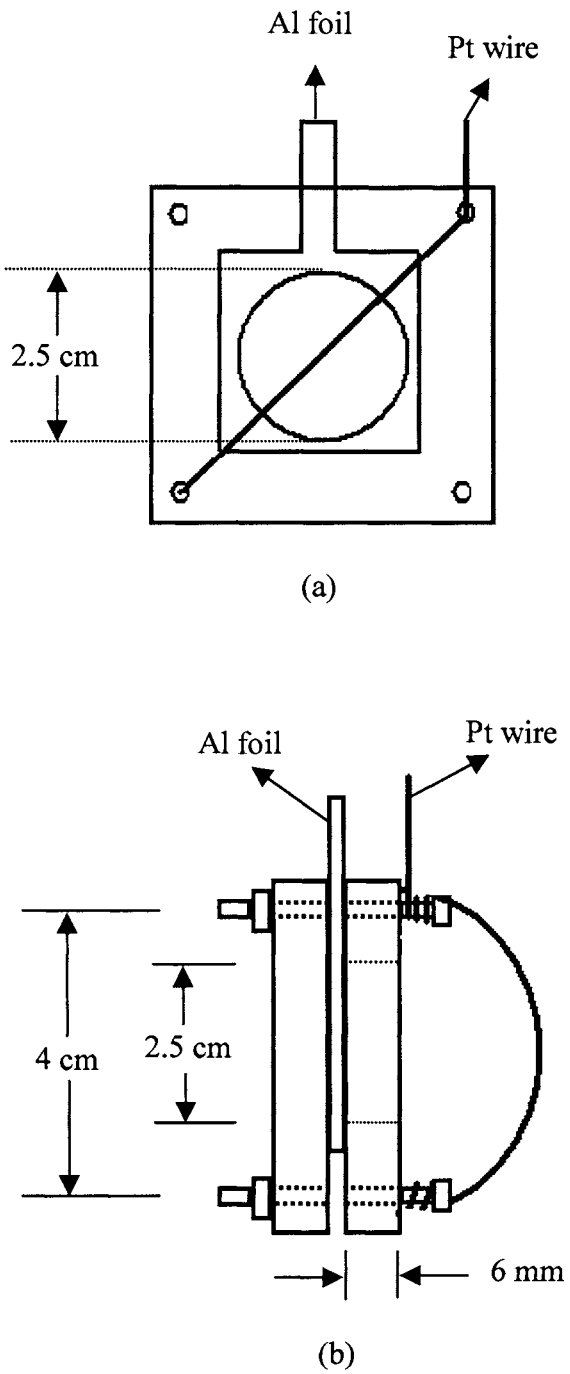

Figure 3.1 Front view (a) and Side view (b) of the electrode holder

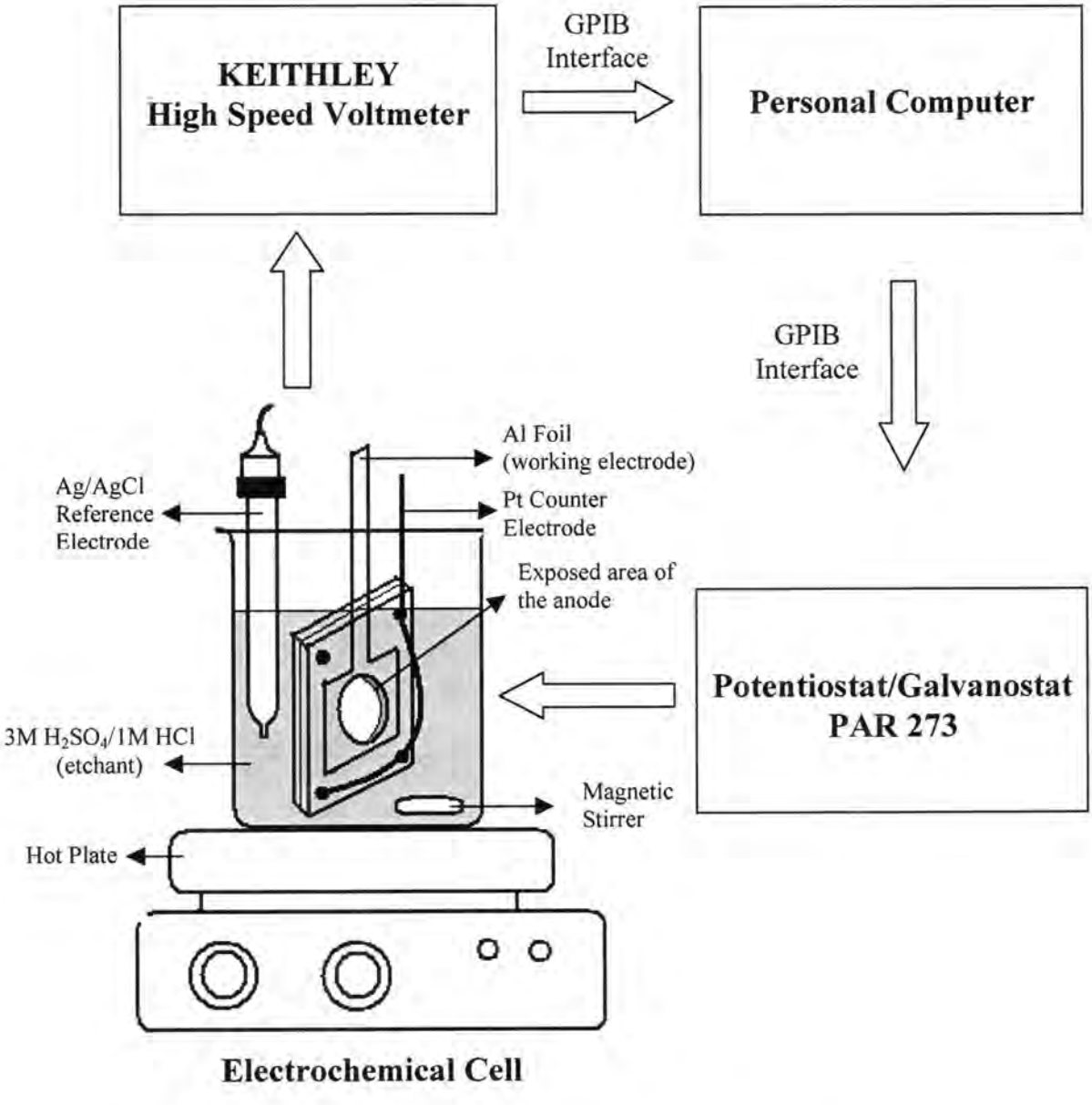

Figure 3.2 Experimental set-up for electrolytic etching of aluminum

3.2. Materials Required and the Procedure

The foils used for etching were 99.98% aluminum foils (TOYO). These foils are 100 μm thick and have a large grain size of about 100 μm formed due to extensive annealing treatments after rolling, e. g. for 5-6 hrs at 600 °C (64). They are generally used in the fabrication of electrolytic capacitors. The etchant was a mixture of 3M sulfuric acid and 1M hydrochloric acid. Solutions for both etching and pretreatment were prepared from reagent grade chemicals and de-ionized water. A Ag/AgCl/4M KCl electrode was used as the reference electrode. It was placed behind the glass holders so as not to disturb the current flow between the counter and the working electrodes. Etching was done at 70 °C with moderate stirring by a magnetic stirrer.

The foils were pretreated in 1M NaOH at room temperature and washed with de-ionized water. Immediately after pretreatment the foils were fitted in the glass holders, and were immersed in the etchant for 10 seconds before actually applying the current. After etching, the foils were rinsed well with de-ionized water and dried. Later they were loaded onto carbon studs and sputter coated with gold to enhance the conductivity of the surface. The morphology of these aluminum surfaces was observed with Scanning Electron Microscope (JOEL 840A).

4. RESULTS AND DISCUSSION

4.1. Focus on Initial Stages of Etching

In order to characterize the kinetics of dissolution processes, and also to obtain information about the process of pit initiation, the early stages of etching was explored by various electrochemical techniques. The results are discussed in the following sections.

4.1.1. Comparison of potential transients for HCl/H_2SO_4 and HCl etchants

A potential transient for etching in 1M HCl/3M H_2SO_4 etchant for 30 s sodium hydroxide pretreatment times is shown in Figure 4.1. The sample was immersed for 10 s in the etchant before actually passing the current. (This is referred to open circuit (O.C) immersion time in the following discussions). The shape of the etching transient is similar to the peak shaped transients obtained earlier by Wiersma and Hebert (47) and Osawa et al. (48), as discussed in the literature review. The etching transient is compared in Figure 4.1 to one measured in 3M H_2SO_4 etchant, using identical pretreatment and electrochemical conditions. Anodic oxide growth and uniform metal dissolution are the only processes which can occur in H_2SO_4 solution (65).

It can be seen from the plot that the potential transients in the two solutions are nearly coincident through most of the etching time when the potential increases towards the maximum. But the SEM images shown in Figure 4.2 clearly reveal pit formation during early etching times, starting from 10 ms. Therefore oxide growth and uniform metal dissolution dominate the applied current through most of the potential rise, even though the pit nucleation process occurs simultaneously.

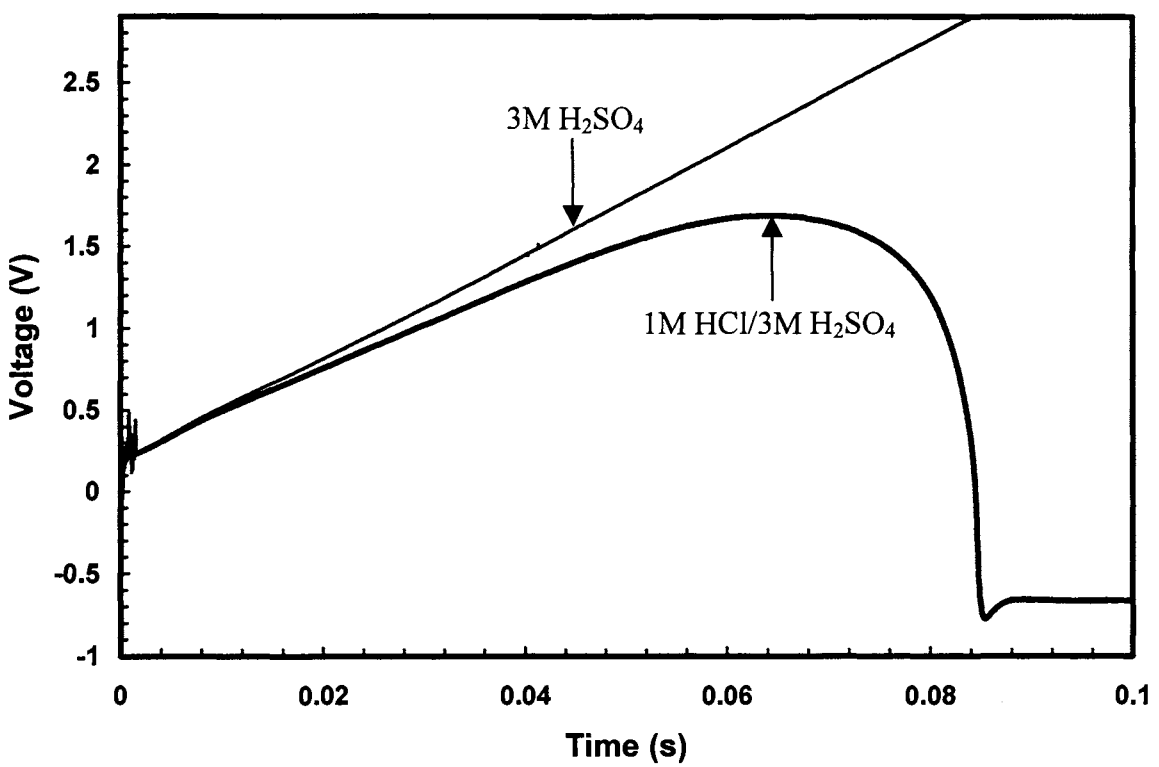

Figure 4.1 Comparison of potential transients for etching done in 1M HCl/3M H_2SO_4 and 3M H_2SO_4. Applied current density 200 mA/cm^2, etchant temperature 70 °C, O.C immersion time 10 s and pretreatment time in NaOH 30 s.

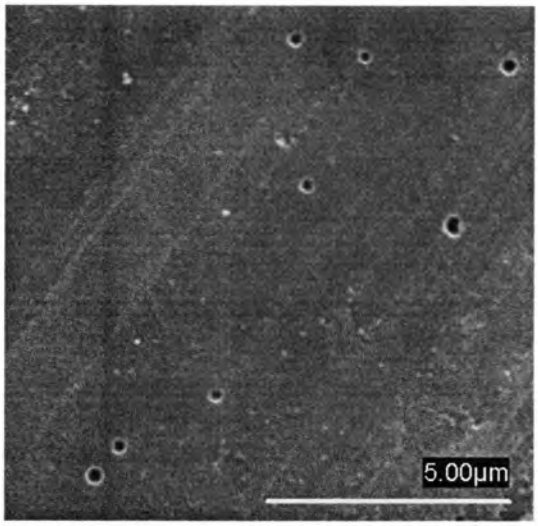

(a) 10 ms

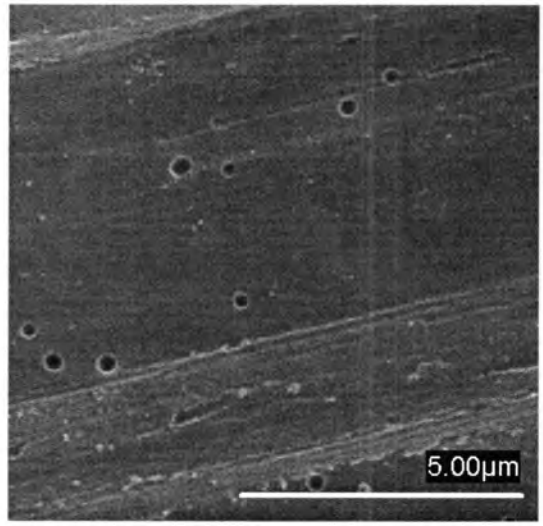

(b) 20 ms

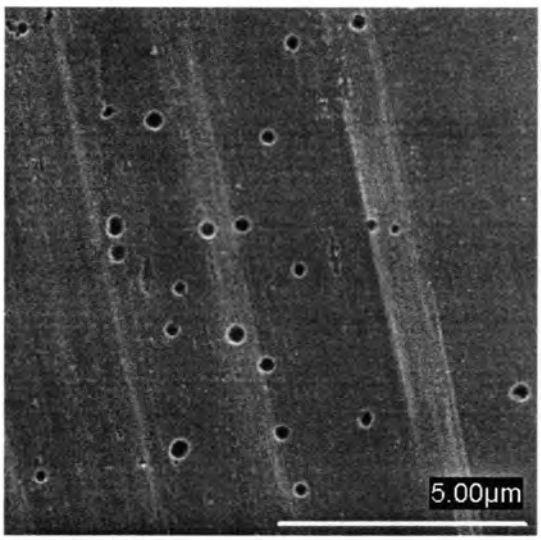

(c) 30 ms

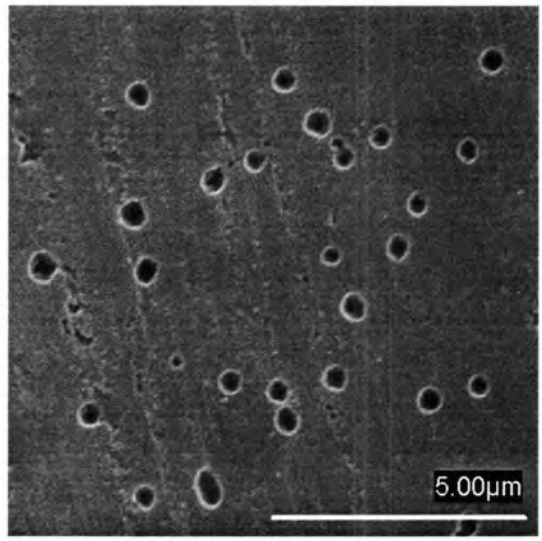

(d) 55 ms

Figure 4.2 SEM images corresponding to various etching times during the initial potential rise. Applied current density 200 mA/cm^2, etchant temperature 70 ^{o}C, NaOH pretreatment time 30 s and O.C immersion time 10 s. Parameter shown is the etching time.

The following schematic elucidates the different electrochemical reactions occurring in the metal/oxide and oxide/solution interfaces.

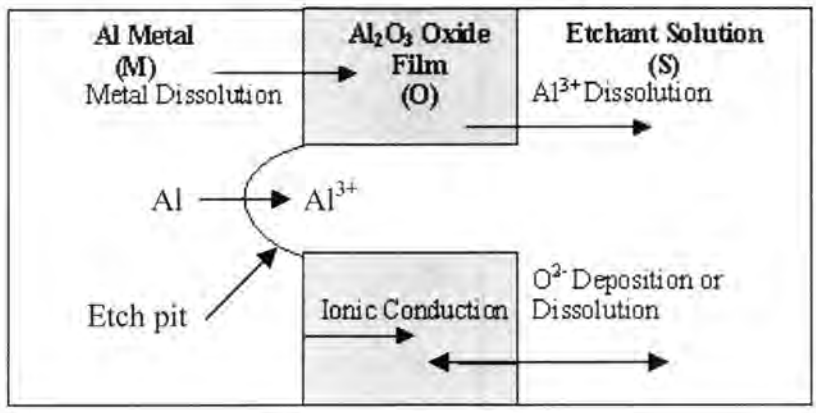

Figure 4.3 Schematic representation of the reactions during etching

M/O Interface

$$2Al + 3O^{2-}(ox) \rightarrow Al_2O_3 + 6e^- \tag{4.1}$$

O/S Interface

$$Al^{3+}(ox) \rightarrow Al^{3+}(aq) \tag{4.2}$$

$$3H_2O \leftrightarrow 3O^{2-}(ox) + 6H^+(aq) \tag{4.3}$$

Etch Pit

$$Al \rightarrow Al^{3+} + 3e^- \tag{4.4}$$

From Figure 4.1, it is evident that at later etching times the potential in mixed acid etchant decreases when compared to that in H_2SO_4 solution, suggesting that uniform corrosion processes which include both anodic oxide growth and uniform metal dissolution are being dominated by pit nucleation. In the next section, experiments are described to help characterize the kinetics of the various electrode processes during the initial transient period.

4.1.2. Current step reduction experiments

Figure 4.4 shows potential transients from experiments in which a sequence of 4 rapid current steps was initiated at various times during etching in HCl/H_2SO_4 etchant. The transients for parallel experiments in 3M H_2SO_4 are shown in Figure 4.5. The high reproducibility of these experiments is obvious from the fact that all these transients can follow the same trace until the initiation of current step sequence. The duration of an individual current step was fixed to be 0.4 ms. It was assumed that this time was small enough to neglect time dependent changes such as oxide or pit growth.

The potentials measured at 0.4 ms after each current step were corrected for the corresponding ohmic drops. In order to evaluate the cell ohmic drop, current step reduction experiments previously done by Wiersma et al. (66) were carried out and the following values for the resistance were obtained.

Table 4.1 Resistance values for the etchants

Etchant	**Resistance (Ω-cm^2)**
1M HCl	1.8872
1M HCl/3M H_2SO_4	0.9516

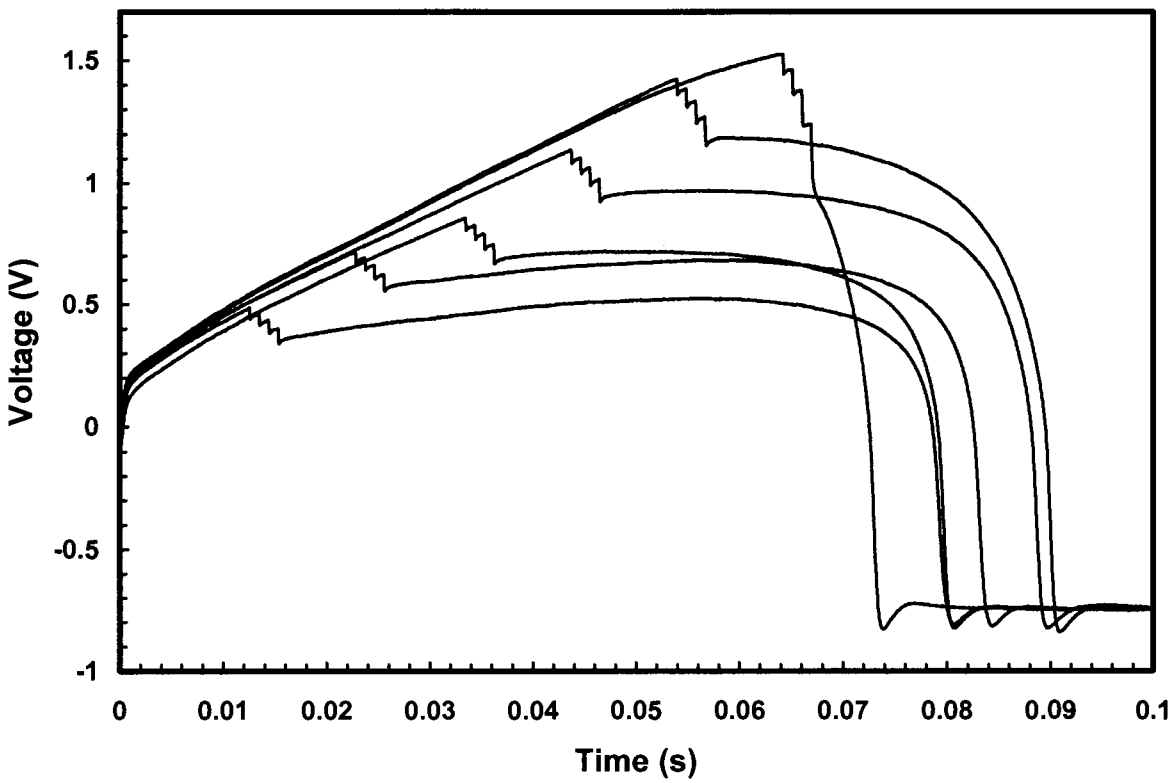

Figure 4.4 Plot showing current step reductions introduced at various times for etching done in 1M HCl/3M H_2SO_4. Current step 25 mA/cm^2, time step 0.4 ms, applied current density 200 mA/cm^2, etchant temperature 70 ^{o}C, O.C immersion time 10 s and pretreatment time 30 s.

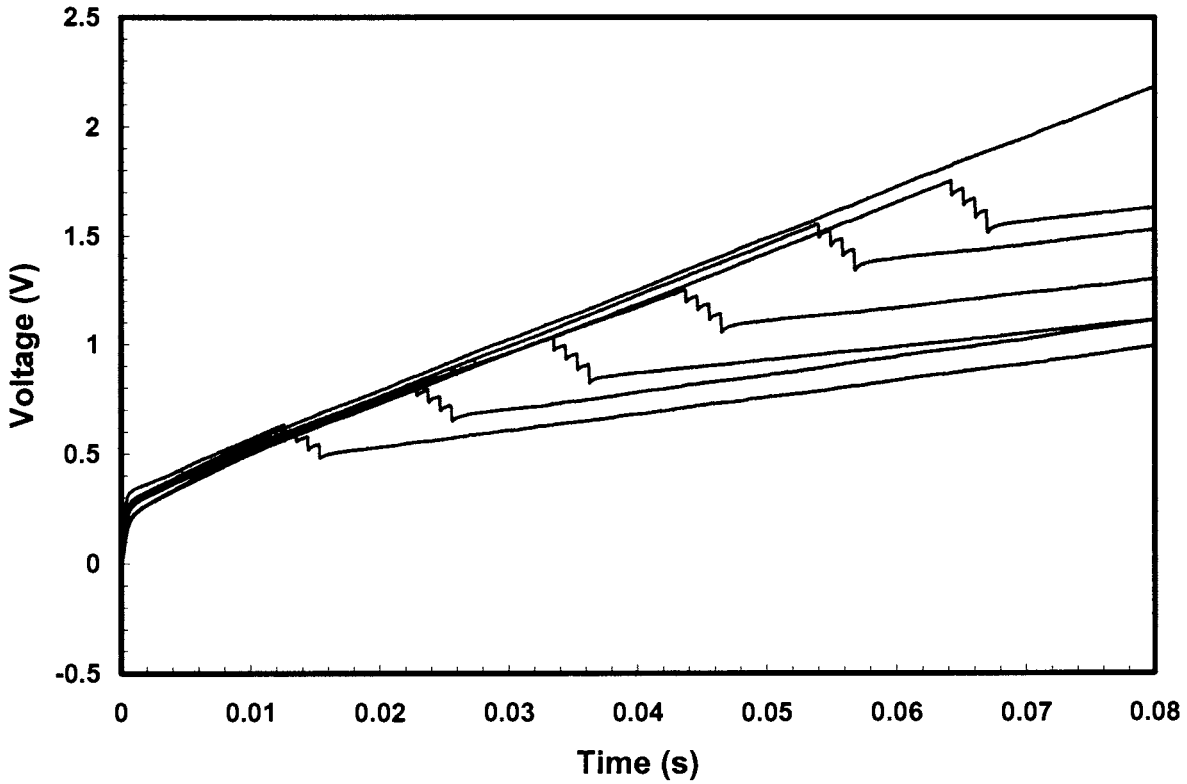

Figure 4.5 Plot showing current step reductions introduced at various times for etching done in 3M H_2SO_4. Current step 25 mA/cm^2, time step 0.4 ms, applied current density 200 mA/cm^2, etchant temperature 70 °C, O.C immersion time 10 s and pretreatment time 30 s.

Based on the conductivity measurements of 108.1 m-mho in HCl/H_2SO_4 solution and 99.3 m-mho in 3M H_2SO_4, the cell resistance for 3M H_2SO_4 etchant was evaluated to be,

$$R_S = 0.9516 \times \frac{108.1}{99.3} = 1.036\ \Omega\text{-cm}^2$$

The ohmic corrected potentials were plotted against the current values as shown in Figures 4.6 and 4.7.

The ionic conduction current density through the oxide film is governed by high-field rate law,

$$i_{an} = i_{ao} \exp\left(\frac{B\phi}{\delta}\right) \tag{4.5}$$

where i_{an} is the ionic conduction current density due to the uniform corrosion processes, ϕ is the potential drop across the oxide film, δ is the oxide film thickness, and i_{ao} and B are kinetic parameters. Using conduction measurements developed by Harkness and Young (67), i_{ao} and B were evaluated to be 1.798×10^{-12} A/cm^2 and 2.99 cm/MV at 70^{O}C respectively.

The potential drop across the oxide film is given by,

$$\phi = E - E_{Al/Al2O3} - iR_S \tag{4.7}$$

where E is the measured potential, iR_S is the cell ohmic drop, $E_{Al/Al2O3}$ is the equilibrium potential for the electrochemical formation of Al_2O_3, which is pH independent. The potential drop across the oxide-solution interface was neglected because it is very small when

compared to ϕ. The value of $E_{Al/Al2O3}$ in strong acidic solutions is –1.51 V at 25 °C (68). This value was extrapolated to 70 °C by using the enthalpy of formation data for the anodic oxide formation reaction

$$2Al + 3H_2O \rightarrow Al_2O_3 + 3H_2 \tag{4.8}$$

The enthalpy values used for the individual components were obtained from Ref. (69). The final value of E_{Al/Al_2O_3} at 70 °C was calculated based on the expression,

$$\Delta H = nF\left[T\left\{\frac{\partial E}{\partial T}\right\}_p - E\right] \tag{4.9}$$

and was found to be –1.518 V, not much different from the value at 25 °C.

Using the high-field rate law, the thickness δ of the oxide film was fitted to the voltage at different etching times corresponding to the beginning of each current step sequence. This specified the current-potential relation expected from ϕ. Since the high field rate law is applicable to the alumina films formed in sulphuric acid (23), the theoretical plots represented as dashed lines were compared to the experimental ones as shown in Figures 4.6 and 4.7 .

Figure 4.6 shows good agreement between the experimental and theoretical plots for etching experiments done in 3M H_2SO_4. This confirms that the high field rate law, Eq. (4.5), models uniform corrosion processes. For etching in HCl/H_2SO_4 solution, the experimental current potential data agree very well with Eq. (4.5) till 45 ms, but deviate significantly at 55 and 65 ms (Figure 4.7). A similar observation was made in the etching transients

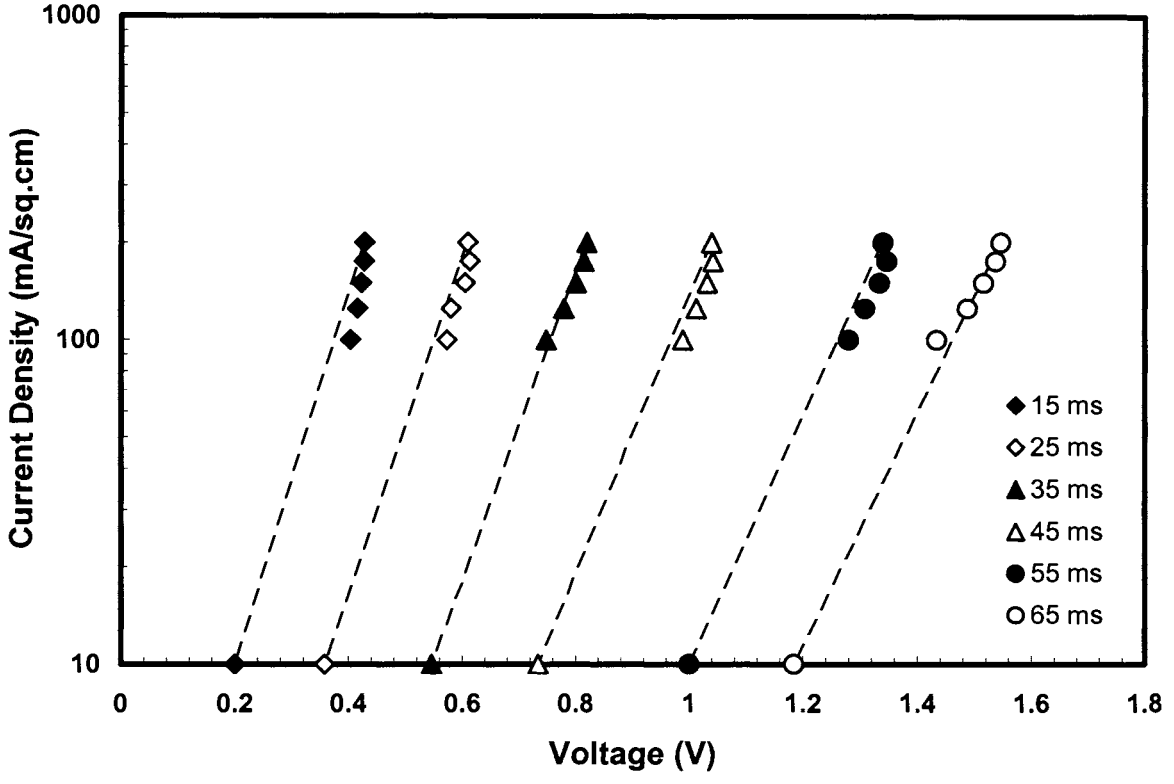

Figure 4.6 Applied current vs potential from the current step experiments of Figure 4.5 in 3M H_2SO_4. Potential is measure at 0.4 ms after current step and corrected for ohmic drop. Dotted lines represent theoretical calculation from Eq. (4.5). Parameter shown is time of first current step in each sequence.

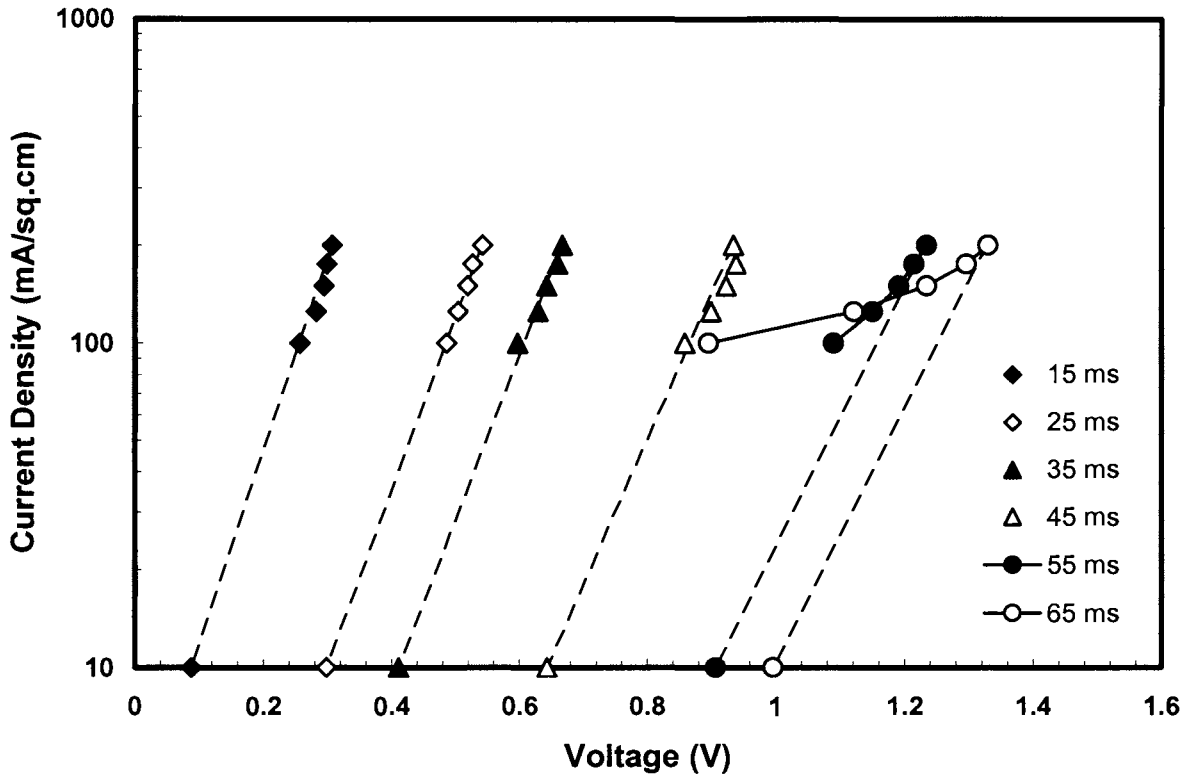

Figure 4.7 Applied current vs potential from the current step experiments of Figure 4.4 in 1M HCl/3M H_2SO_4. Potential is measure at 0.4 ms after current step and corrected for ohmic drop. Dotted lines represent theoretical calculation from Eq. (4.5). Parameter shown is time of first current step in each sequence.

shown in Figure 4.1; the potential transients for HCl/H_2SO_4 and HCl solutions agree until 35 ms, but deviate significantly at later times. The reduced potential at later etching times in HCl/H_2SO_4 solution suggests that pitting dominates the uniform corrosion processes and supplies most of the applied current by active metal dissolution.

The current-potential relation corresponding to these times in Fig. 4.7 may be interpreted as kinetics of metal dissolution from pits. The next step in studying the etching behavior of aluminum is to explore the mechanism of pit dissolution, which is discussed in the following section.

4.2. Evaluation of Mean Pit Dissolution Current Density from Etching transient and SEM Results

The rate of oxide film growth in H_2SO_4 solution is given by,

$$\frac{d\delta}{dt} = \frac{\varepsilon i_{an}}{6FC_{ox}} \tag{4.10}$$

where i_{an} is the current density due to the uniform corrosion processes, δ is the oxide film thickness, C_{ox} is the concentration of Al_2O_3 in the oxide film and ε is the current efficiency of oxide growth. In case of H_2SO_4 solution, i_{an} can be replaced by the applied current i_{app} since the entire applied current in this case is supplied by the uniform corrosion process. Using Eq. (4.5), $\frac{d\delta}{dt}$ can be substituted by $\frac{dE}{dt}$ which represents the instantaneous slope of the potential transient. The following expression is obtained for the efficiency of oxide film growth

$$\varepsilon = \frac{6FC_{ox}B}{i_{an}\ln\left(\frac{i_{an}}{i_{ao}}\right)}\frac{dE}{dt} \tag{4.11}$$

The current efficiency for H_2SO_4 solution was evaluated for different times. Since the pH of the sulfuric acid solution and HCl-H_2SO_4 etchant are similar, it was assumed that the same current efficiencies were valid in the etchant. The instantaneous slope values from the potential transients were substituted for $\frac{dE}{dt}$ in Eq. (4.11) and the equation was used to evaluate the uniform corrosion current density at different etching times.

The applied current density is the overall contribution from capacitive charging current $C\frac{dE}{dt}$, uniform corrosion current i_{an} and the pit dissolution current i_{pit}

$$i_{app} = C\frac{dE}{dt} + i_{an} + i_{pit} \tag{4.12}$$

Thus the overall pit current density was found by subtracting the uniform corrosion current density from the applied current density. The capacitive charging current becomes negligible except for the first few microseconds of the potential overshoot and for few microseconds when the potential drops abruptly from the peak value to a steady state value.

SEM images of the foil surface were obtained for the etching times listed in Table 4.2 (Figure 4.2). It is evident from these images that pits at these etching times are hemispherical in shape. The total pitted area is then $2\pi\langle r^2\rangle n_{pit}$, where $\langle r^2\rangle$ is the mean square pit depth and n_{pit} is the pit density. The pit population used in evaluating $\langle r^2\rangle$ varied between 30 and 85. About 5 micrographs taken at individual etching times were used in evaluating n_{pit}. The pit population for the different etching times varied between 20 and 100. Figures 4.8 and 4.9 show the variation of $\langle r^2\rangle$ and n_{pit} along with the confidence limits for increasing etching time. In the SEM images, the pits were easily distinguished by dark spots, in contrast with much lighter regions that represent the foil surface. In evaluating $\langle r^2\rangle$ and n_{pit} from the SEM images, the pits that appeared as relatively lighter spots were considered to be shallow passivated ones and hence were neglected in the calculations. The statistical analysis

Table 4.2 Results from dissolution rate measurements.

Etching Time (ms)	Efficiency	Uniform Corrosion Current Density (A/cm^2)	Mean-square Pit Depth (μm^2)	Pit Number Density ($x\ 10^6\ cm^{-2}$)	Mean Dissolution Current Density (A/cm^2)
10	0.29	0.183	0.0073	4.16	8.91
20	0.25	0.172	0.012	4.58	8.11
30	0.25	0.162	0.025	4.92	4.92
40	0.26	0.155	0.031	6.91	3.35
55	0.26	0.096	0.058	7.06	4.04
65	0.26	0.0065			

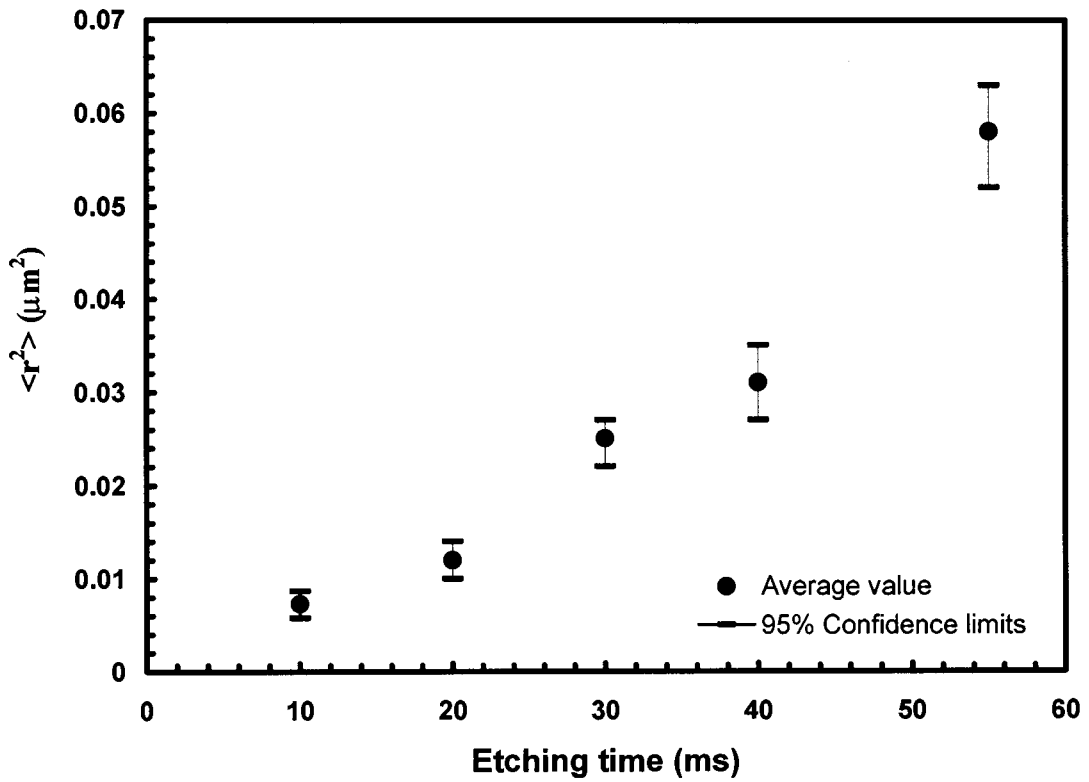

Figure 4.8 Variation of mean square pit depth $\langle r^2 \rangle$ with etching time. Etching current density 200 mA/cm^2, etchant temperature 70 °C, NaOH pretreatment 30 s and O.C immersion time 10 s.

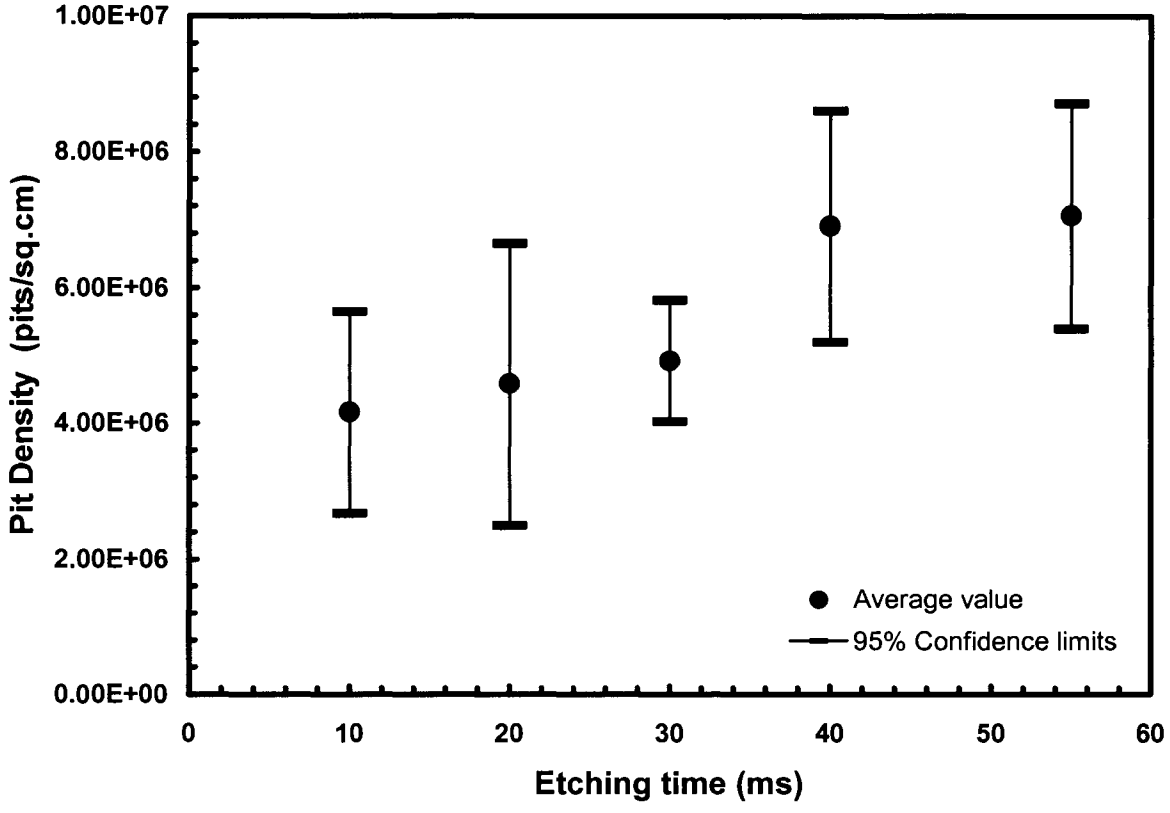

Figure 4.9 Variation of pit density with etching time. Etching current density 200 mA/cm^2, etchant temperature 70 ^{o}C, NaOH pretreatment 30 s and O.C immersion time 10 s.

assumed normal distributions for the samples. The mean pit dissolution current density i_d was evaluated by dividing the overall pit current density i_{pit} by the total pit area.

The confidence limit calculation was based on the following expressions

$$\overline{\mu} = \mu_1 \times \mu_2 \tag{4.13}$$

$$\overline{\sigma^2} = \left(\frac{\sigma_1^2}{n_1} + \mu_1^2\right) \times \left(\frac{\sigma_2^2}{n_2} + \mu_2^2\right) - \mu_1^2 \mu_2^2 \tag{4.14}$$

The 95% confidence limits of i_d were evaluated as,

$$\text{Lower limit} = \frac{i_{pit}}{2\pi\left(\overline{\mu} + 1.96\overline{\sigma}\right)} \tag{4.15}$$

$$\text{Upper limit} = \frac{i_{pit}}{2\pi\left(\overline{\mu} - 1.96\overline{\sigma}\right)} \tag{4.16}$$

where μ_1, μ_2 *and* $\overline{\mu}$ are the mean values and σ_1, σ_2 *and* $\overline{\sigma}$ are the standard deviations of n_{pit}, $\langle r^2 \rangle$ and $n_{pit}\langle r^2 \rangle$ respectively. n_1 represents the total number of micrographs used for n_{pit} evaluation and n_2 refers to the total number of pits considered in $\langle r^2 \rangle$ evaluation. Figure 4.10 shows the variation of i_d with confidence limits at different etching times, and the values are tabulated in Table 4.3. It is evident from the table that the mean pit dissolution current density lies in the range of 3-9 A/cm^2. This is consistent with earlier work in HCl etchant at 70 ^{0}C (47), in which a mean value of 6 A/cm^2 was reported. The same value was also obtained for the tunnel etching experiments done in 1N HCl at 65 ^{0}C. Thus the etch

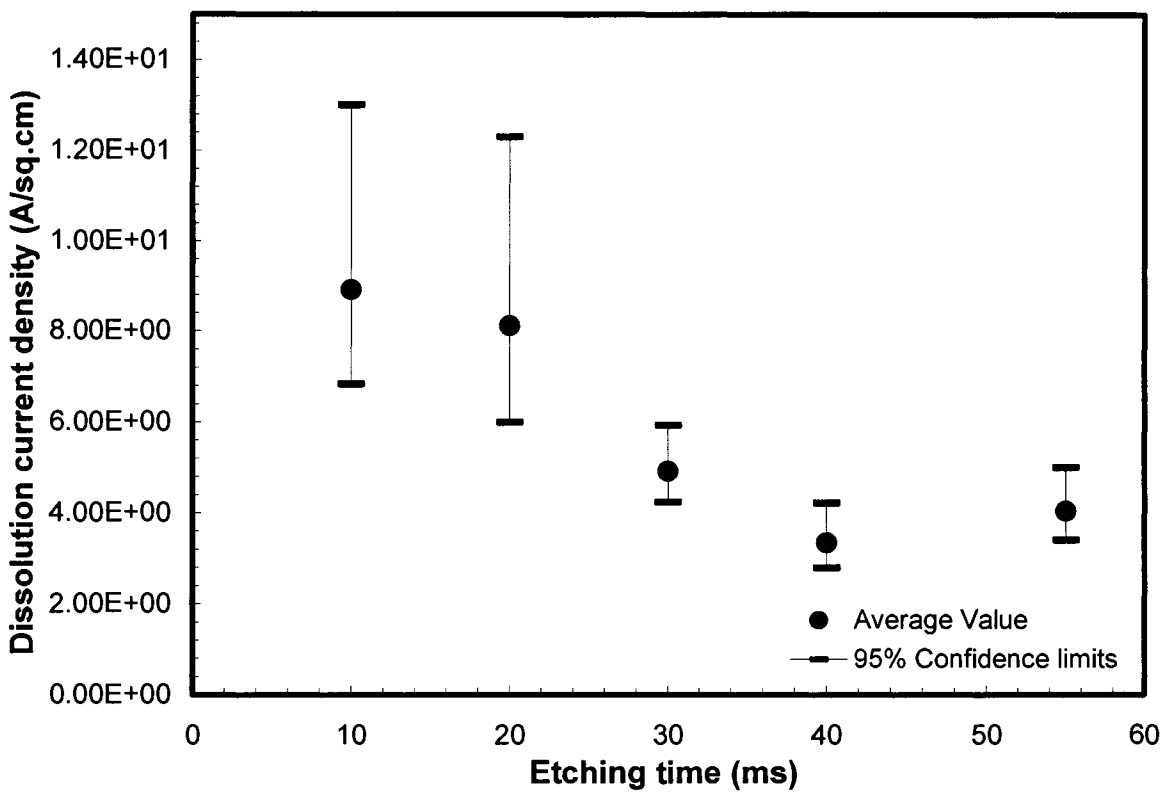

Figure 4.10 Plot showing the dissolution current density evaluated at different etching times. Etching current density 200 mA/cm^2, etchant temperature 70 ^{o}C, NaOH pretreatment 30 s and O.C immersion time 10 s.

tunnels which grow at a very low potential of about -0.8 V have the same metal dissolution current density value as that of the etch pits which usually nucleate at a much higher potential of 0.3-3 V. This suggests that the metal dissolution rate is potential independent. But the dissolution rate exhibits a Tafel type dependence in the current step reduction experiments in Figure 4.7. Also the current pulse experiments done during tunnel growth in HCl etchant (70) show a Tafel-like dependence of the metal dissolution rate on the measured voltage. In order to further investigate these contradictory results, similar current pulse experiments were done using the HCl-H_2SO_4 etchant, as discussed in the following section.

4.2.1. Dissolution rate measurement in etch tunnels using current pulse experiments

Figure 4.11 represents the current waveform for the pulse experiments done in HCl-H_2SO_4 etchant. As shown in the diagram, aluminum foils pretreated in NaOH solution for 20 minutes were etched at an applied current density i_{a1} of 200 mA/cm^2. The samples were etched for different times t_e corresponding to 1 s, 5 s and 10 s. This produced etch tunnels of approximately uniform length whose growth rate was measured to be 2.1 μm/s in HCl-H_2SO_4 etchant using the oxide-replication technique of Hebert (71). Immediately after time period t_e the current density was reduced to i_{a2}, which made the potential more negative than the repassivation potential, below which active metal dissolution is not maintained. This reduced potential passivated part of the active tunnel surface. The applied current was maintained at i_{a2} for 12 ms, followed by an anodic pulse to the higher value i_{a3}. Figures 4.12 and 4.13 represent the potential transients at times near the current step from i_{a2} to i_{a3}, for i_{a1} = 40 mA/cm^2 and t_e = 1 s. These transients are for different values of i_{a2} and i_{a3}. All the transients exhibit a rapid increase in potential to a peak value within 0.2 ms.

To help interpret the transients for current pulse experiments, they were compared to transients for current interruption experiments. The interruption followed the waveform of Figure 4.11 with $i_{a2} = 0$ mA/cm^2. Figure 4.14 shows a comparison of these transients with the

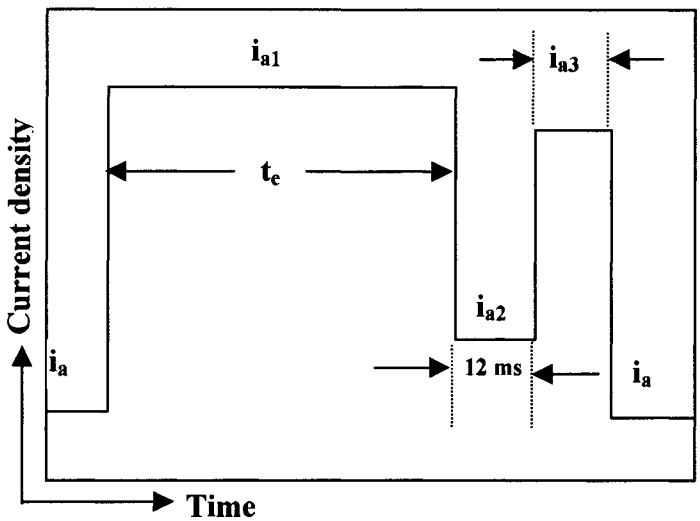

Figure 4.11 Schematic representation of current waveform for current step reduction.

transients obtained for the current reduction experiments represented in Figure 4.12. It can be seen that the peak potential for the current interruption experiments is 60-200 mV greater than that of current reduction experiments. It was already shown by Tak et al. (70) that during the brief current interruption with $i_{a2} = 0$ mA/cm^2 the entire tunnel tip is passivated, and later the current during the anodic pulse is supplied by pit nucleation and uniform corrosion processes. But the significantly higher potential required to activate these two current sources indicates that in current reduction experiments, the current density during i_{a3} was supplied by active metal dissolution from areas not passivated during the current reduction.

The dissolution current density from the patches, denoted as patch current density i_{p2} was evaluated based on the expression developed by Tak et al. (70) given as,

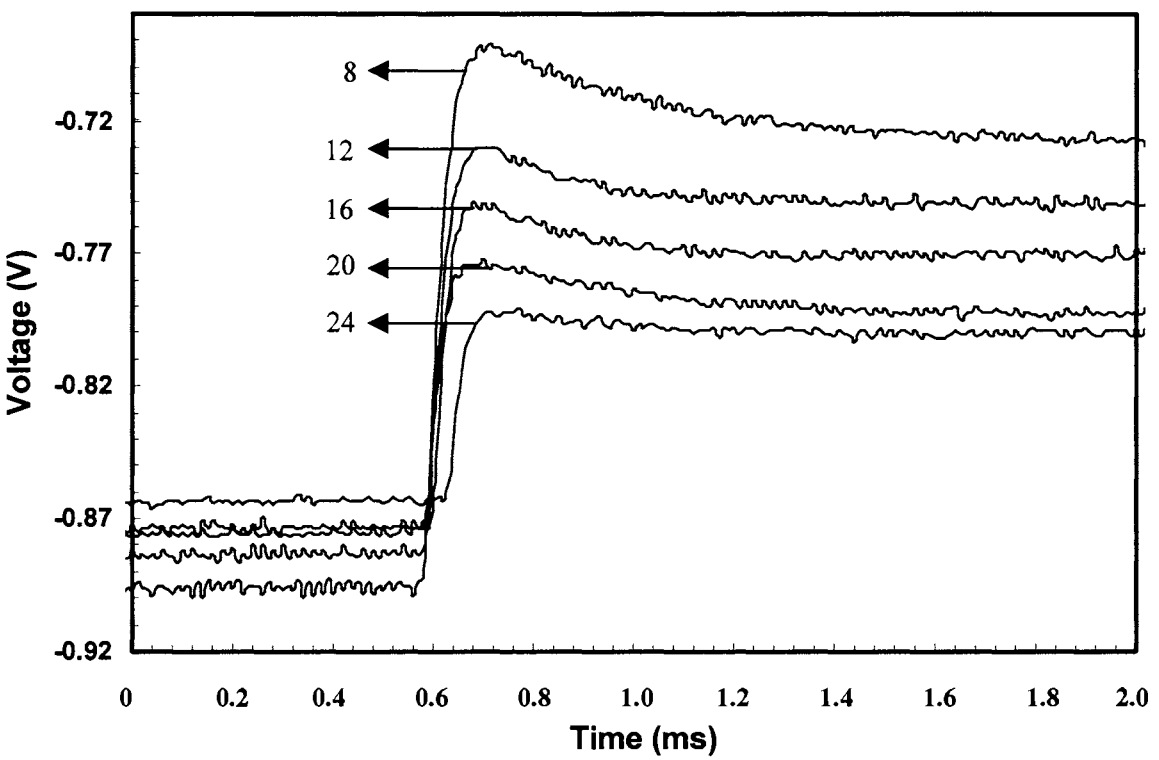

Figure 4.12 Potential transients for various values of i_{a2} in mA/cm^2 (parameter shown in plot), during anodic pulses following pulsed current reductions. i_{a1}= i_{a3}= 40 mA/cm^2. t_e 1 s.

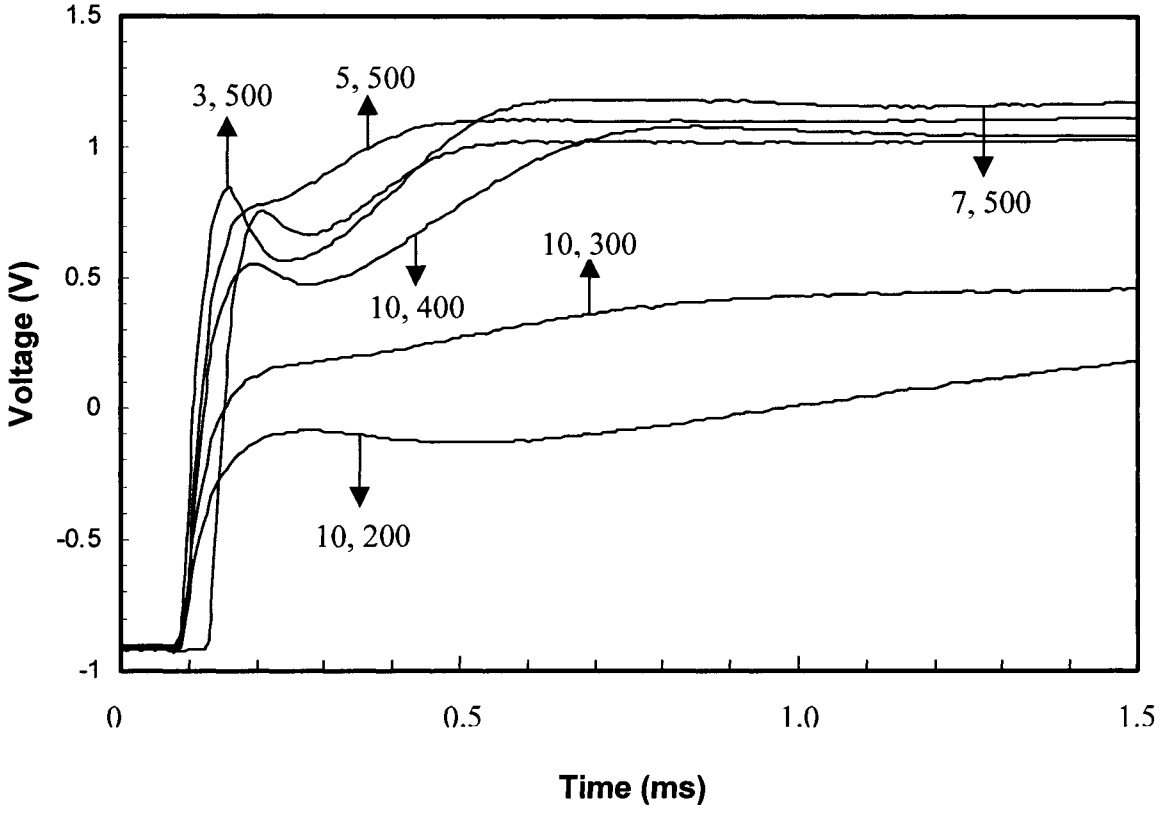

Figure 4.13 Potential transients for various values of i_{a2} , i_{a3} in mA/cm^2 (parameters shown in plot respectively). i_{a1} = 40 mA/cm^2. t_e 1 s.

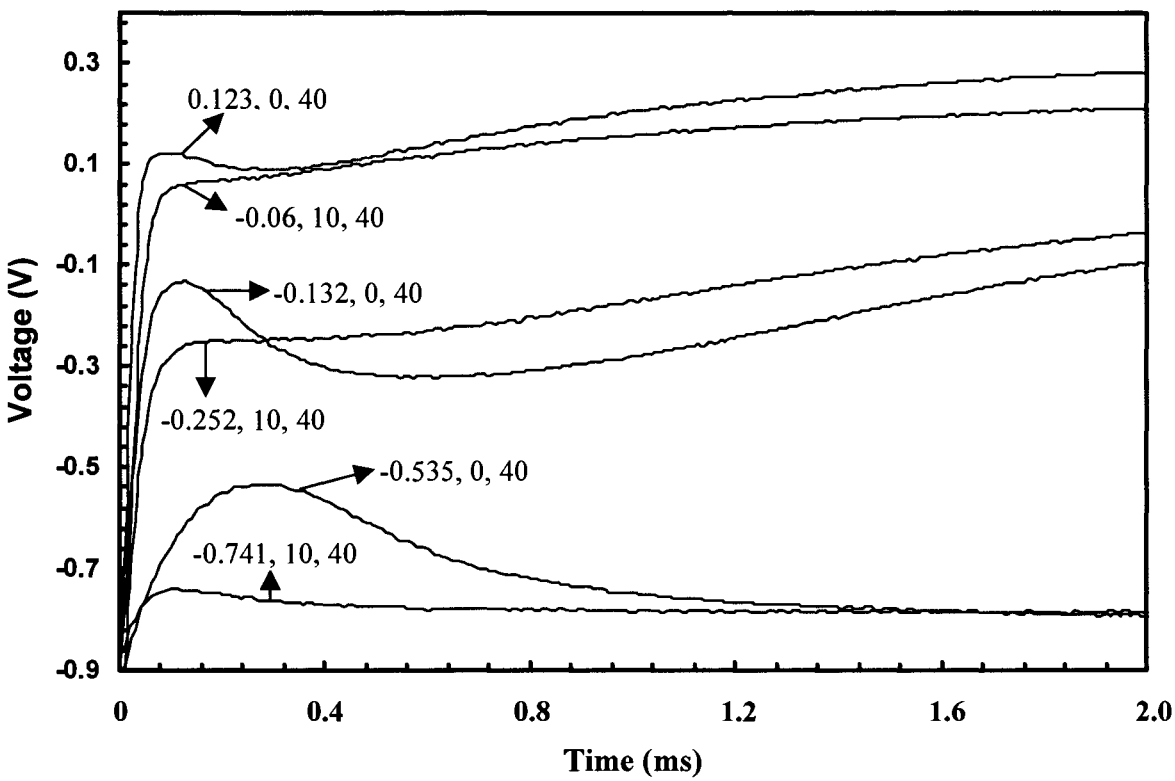

Figure 4.14 Comparison of potential transients corresponding to current interruption experiments (i_{a2} = 0 mA/cm^2) and current reduction experiments (i_{a2} = 10 mA/cm^2). i_{a1} = 40 mA/cm^2, t_e 5 s. Parameters shown represent maximum potential, i_{a2} and i_{a3} respectively.

$$i_{p2} = i_{p1} \frac{(i_{a3} / i_{a1})}{(i_{a2} / i_{a1})} \tag{4.17}$$

i_{p1} represents the constant patch current density before and during the current step reduction, $\frac{i_{a2}}{i_{a1}}$ is the ratio of the area passivated to the entire tunnel tip area, and $\frac{i_{a3}}{i_{a1}}$ represents the increase in total current during the anodic pulse.

The peak potential was corrected for the cell ohmic drop evaluated previously. In order to evaluate the ohmic drop of the solution inside the tunnels, the potential upon stepping from i_{a1} to i_{a2} was carefully analyzed as described already by Wiersma et al. (66). The potential transient following this current step is given in Figure 4.15. The plot shows that the potential drops to a minimum value when the current is decreased from i_{a1} to i_{a2}, and later slowly increases to a steady state value. It was explained by the authors that the difference between the minimum value E_{min} and the steady state value E_o (indicated as ΔE) represents the sum of the ohmic drop in the solution inside the tunnels, and a surface over-potential at the tunnel tip. The current step was introduced at different etching times in order to vary the length of the etch tunnels, and the ΔE values were plotted against the tunnel length as shown in Figure 4.16. The figure indicates that the ohmic drop inside the tunnels is insignificant, since ΔE is approximately constant for varying tunnel lengths.

Current potential data obtained in experiments with various t_e, i_{a2} and i_{a3} are plotted in Figure 4.17, along with those found earlier with HCl etchant. In the present experiments the dissolution current density values were extended to the order of 1000 A/cm^2, in contrast to the work of Tak et al., wherein the maximum value was less then 100 A/cm^2. The plot

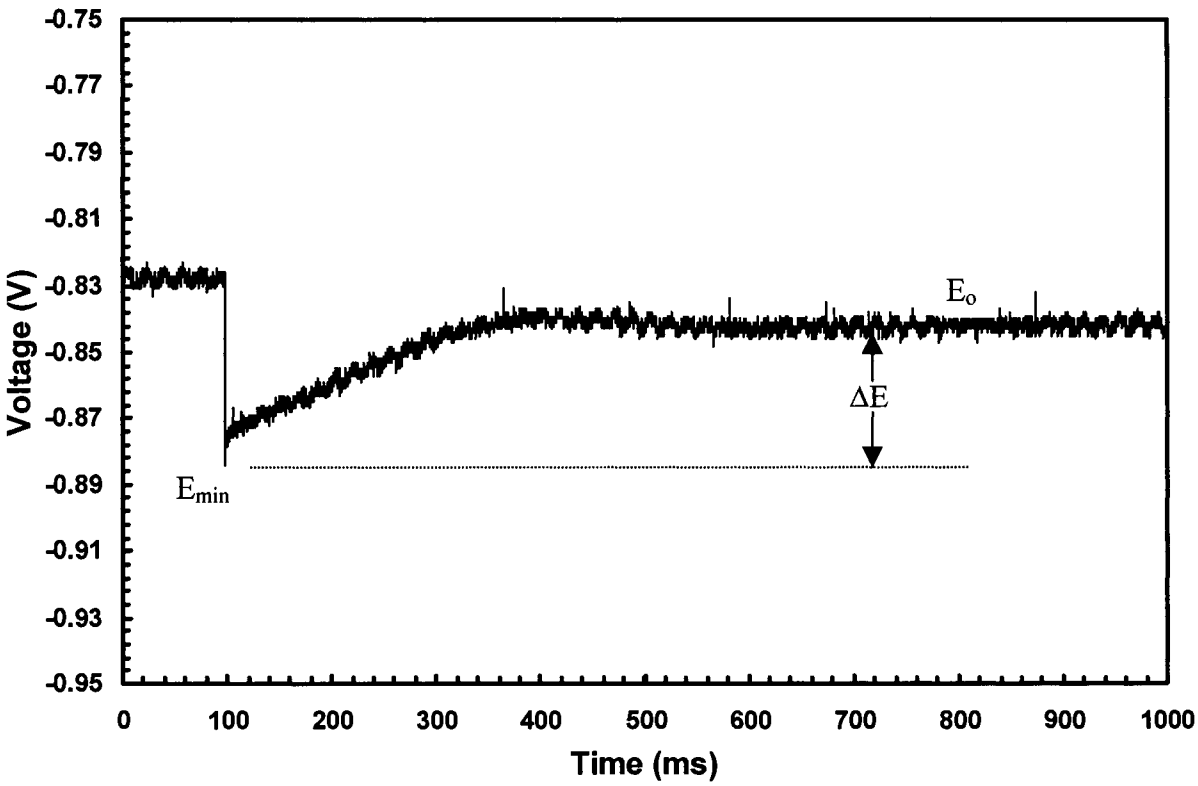

Figure 4.15 Potential transient after 40% reduction on base applied current density of 40 mA/cm^2. Temperature 70 °C, NaOH pretreatment time 20 min, O.C immersion time 10 s, step time 10 s.

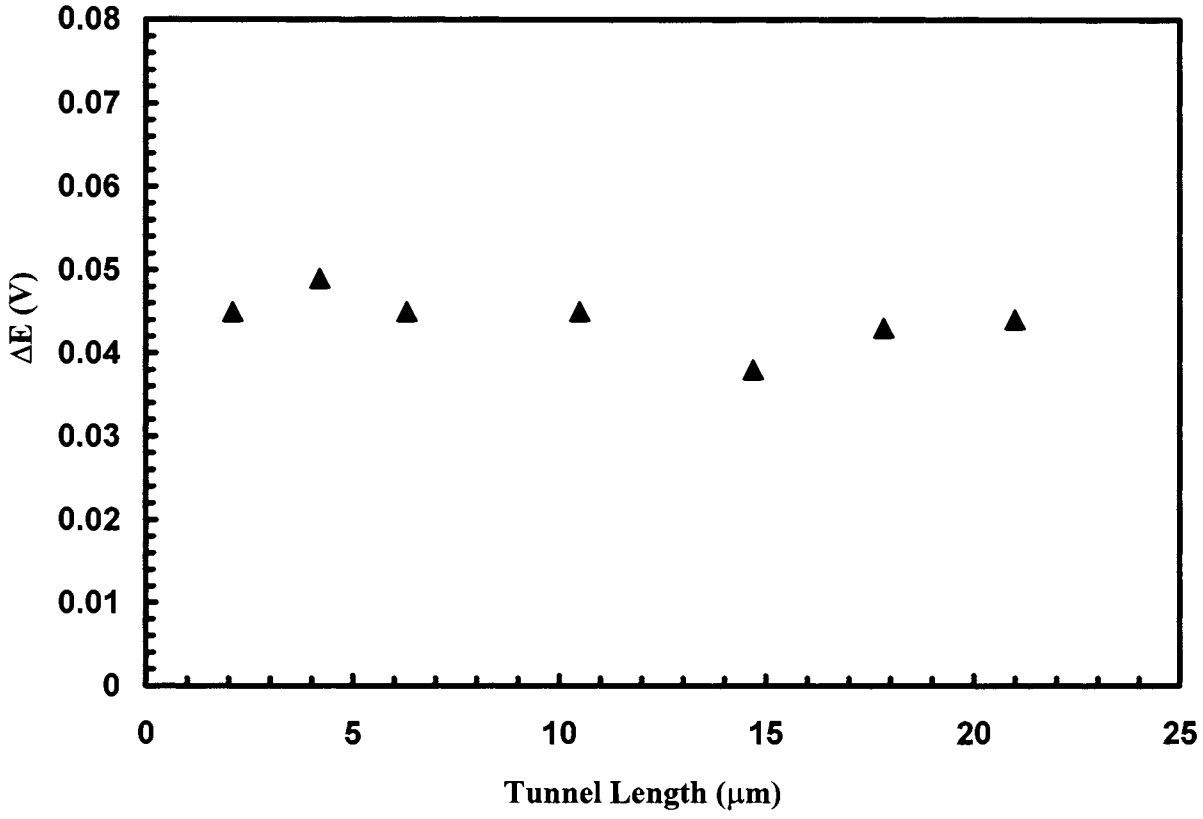

Figure 4.16 Variation of potential drop ΔE with tunnel length before current step. 40% current reductions. Applied current density 40 mA/cm^2, temperature 70 °C, NaOH pretreatment time 20 min, O.C immersion time 10 s.

reveals that all the experiments in 1M HCl and 1M HCl-3M H_2SO_4 follow the same current-potential dependence.

The current potential data could be fitted to a simple Butler-Volmer kinetic expression,

$$i = i_{1o} + i_{2o}\left[\exp\left(b_2^+(E - E_o)\right) - \exp\left(-b_2^-(E - E_o)\right)\right] \tag{4.18}$$

where E represents the electrode potential and E_O is an empirically fit potential. The significance of the additive current density i_{1O}, and the empirical potential coefficients b_2^+ and b_2^- used in the above equation is discussed in the following section. The parameter values obtained by fitting are listed out in Table 4.4. i_{1O} was set to 6.1 A/cm^2 which represents the constant metal dissolution rate for the steady-state tunnel growth. The value of the Tafel coefficient b_2^+ = 1.55 V^{-1} is consistent with the value of the Tafel slope 1.6 V^{-1} from the current step experiments in Figure 4.7, at the 65 ms etching time. This shows that the potential dependence of the dissolution current density in both etch pits and tunnels are similar, as revealed by current step experiments. On the other hand, Table 4.3 shows approximately constant values of dissolution current densities for etching times of 10-65 ms corresponding to pit growth, which are quite consistent with the value of 6.1 A/cm^2 measured in a variety of ways by Hebert and Alkire during tunnel growth.

Table 4.3 Fit values of the parameters used in Eq. (4.18)

Parameter	**Fit value**
i_{2o}	43 ± 8.4 A/cm^2
b_2^+	1.55 ± 0.11 V^{-1}
b_2^-	3.9 ± 4.8 V^{-1}
E_o	0.816 ± 0.061 V

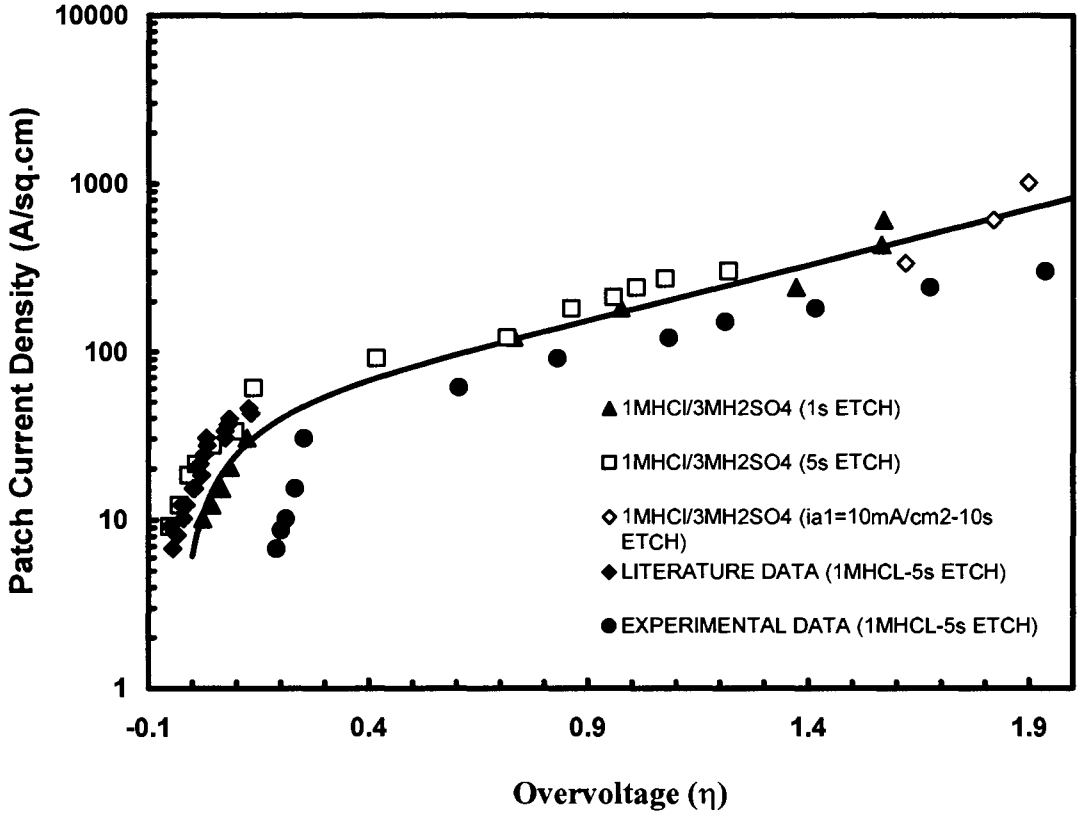

Figure 4.17 Plot showing the relationship between patch current density and the overpotential evaluated from the maximum potential in the potential transient. Solid line shows the fit to experimental data obtained by varying the values of i_{a1}, i_{a2} & i_{a3}. The fitted values are E_o 0.816 V, i_{1O} 6.1 A/cm^2, i_{2o} 37 A/cm^2, b_2^+ 1.55 V^{-1}, b_2^- 3.9 V^{-1}.

These results suggest that the apparent contradiction between the constant and potential dependant current densities is not due to different dissolution process in pits and tunnels. It is concluded that the experimental time scale during which the dissolution rate measurements are carried out is the only factor that leads to these potential-dependent vs constant dissolution rates. It is evident from Figures 4.7 and 4.17 that when this time scale is within 1 ms after the initiation of current step, there is a prominent Tafel like dependence of the dissolution current density with the potential. On the other hand, the dissolution rate measurements that are made at much longer time scales after the current step disturbance, as shown in Table 4.3, yield an approximately constant value of about 6.1 A/cm^2, independent of the potential. In order to elucidate the time scale dependant dissolution kinetics, a kinetic model based on the Vetter-Gorn kinetic model is developed in the following section.

4.2.2. Kinetic model for dissolution kinetics

4.2.2.1. Description of the various electrochemical reactions involved

The Vetter-Gorn model describes the kinetics of oxide layer formation on a metal based on the individual rates of dissolution of metal ions, and deposition or dissolution of oxygen ions, both occurring in the metal-oxide/solution interface (3, 4). The corrosion and the oxide formation processes are schematically shown in Figure 4.3, and are described by Eqs. 4.2 and 4.3 respectively.

In their earlier work, Beck and Alkire (57) proposed the formation of salt film which covers the entire dissolving surface of the pits. The precipitation of the salt film occurs due to the exceedingly high current densities inside the etch pits. Beck (56) explained the formation of a continuous aluminum chloride salt film over the dissolving surface of the etch pits that

initiate during aluminum corrosion. The Vetter-Gorn model can be presumed to be a general model for describing dissolution kinetics in the presence of films formed from corrosion products, and hence the kinetic model developed in this section is based on it. Also, the Vetter-Gorn model yields potential independent current densities under quasi-steady state conditions and potential-dependent behavior in experiments with small time scales. This is similar to the trend observed for the dissolution rate measurements, and further validates our presumption.

Based on the earlier study of Beck and Alkire (57), which stated that the salt films inside the etch pits are tens to hundreds of angstroms thick for some systems, it is assumed that the etch pits in aluminum are covered by a monolayer or multilayer metal salt film Figure 4.18 shows the various electrochemical reactions associated with the salt film present inside the etch pits.

As shown in the figure, the metal actively dissolves at the metal/salt-film interface and combines with the chloride ions from the solution to form the $AlCl_3$ salt-film. The migration of the Al^{3+} ions through the film follows high-field conduction,

$$i_f = i_{f0} \exp\left(\frac{B_f \phi}{\delta}\right) \tag{4.19}$$

which is same as that of Eq. (4.5), but all the parameters refer to the salt film instead of the oxide film. The reactions occurring at the salt-film/solution interface are metal ion dissolution ,

$$Al^{3+}(f) \rightarrow Al^{3+}(aq) \tag{4.20}$$

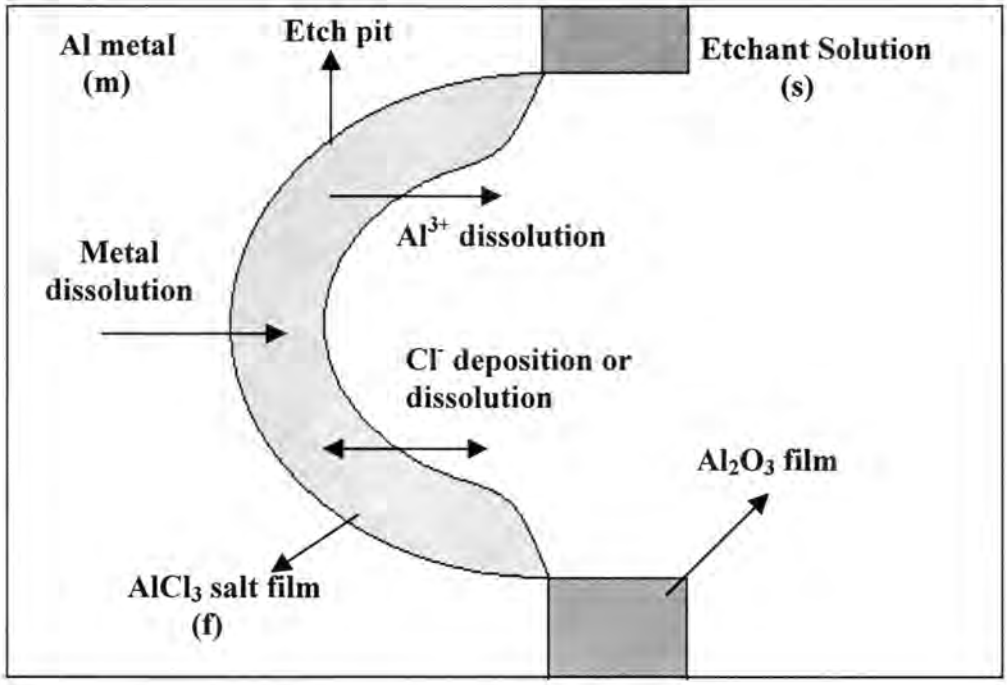

Figure 4.18 Schematic representation of the reactions inside etch pit

and the deposition or dissolution of chloride ions,

$$Cl^{-}(f) \leftrightarrow Cl(aq) \tag{4.21}$$

These two reactions are exactly similar to the metal ion dissolution and O^{2-} deposition or dissolution reactions that occur in the oxide-film/solution interface during etching. As explained by Vetter, for reaction (4.20) to be in equilibrium, the Al^{3+} concentration in the solution near the salt- film/solution interface should be near the solubility product of the salt. Since the concentration of Al^{3+} ions is low, it is assumed that the reverse deposition process in Eq. (4.20) is negligible. The reaction rates for Eqs. (4.20) and (4.21) are dependent on the

potential drop at the salt-film/solution interface which is represented by the overpotential η with respect to the equilibrium of chloride ions.

The current density due to the Al^{3+} dissolution is represented by the Tafel equation,

$$i_C(\eta) = i_{C0} \exp(b_C \eta) \tag{4.22}$$

and that of chloride ion transfer is given by the Butler-Volmer equation,

$$i_L(\eta) = i_{L0}\left[\exp\left(b_L^+ \eta\right) - \exp\left(-b_L^- \eta\right)\right] \tag{4.23}$$

where b_C, b_L^+ and b_L^- are the potential co-efficients, and i_{C0} and i_{L0} are the pre-exponential current densities in the kinetic equations.

In the Vetter-Gorn model it was assumed that the oxide film covering the metal maintains an approximately constant stoichiometric proportion of the oxygen ions. The same assumption is made for the chloride ions in the salt-film. Thus the growth rate of the salt-film can be related to the rate of chloride ion transfer,

$$\frac{d\delta}{dt} = \frac{i_L(\eta)}{3FC_F} \tag{4.24}$$

where C_F refers to the concentration of $AlCl_3$ in the salt-film. The conduction current density through the salt-film i_f, and the interfacial current densities i_C and i_L should satisfy the condition for current continuity at the salt-film/solution interface,

$$i = i_f(\phi) = i_L(\eta) + i_C(\eta) \tag{4.25}$$

The measured potential is given as the sum of the equilibrium potential at the metal/salt-film interface $E^{o}_{Al/AlCl_3}$, the overpotential at the salt-film/solution interface η, the potential drop across the salt film ϕ and the ohmic potential drop in the solution,

$$E = E^{o}_{Al/AlCl_3} + \phi + \eta + iR_S \tag{4.26}$$

similar to Eq. (4.7). The term $E^{o}_{Al/AlCl_3}$ is included in the above expression because it is assumed that the metal atoms are in equilibrium with the metal ions in the salt film.

4.2.2.2. Kinetic expressions for the two limiting cases of the model

The time scale of the dissolution rate measurement determines the limiting case for the kinetic model being developed. If the experimental time scale is long enough, then the chloride ion transfer reaction between the salt film and the solution attains equilibrium and thus the overpotential η at the salt-film/solution interface becomes zero. When η=0, then according to Eq. (4.22) the dissolution current density i_C becomes i_{C0} and the rate of chloride ion transfer becomes zero as described in Eq. (4.23). Thus a constant dissolution current density $i = i_{C0}$ is always obtained, as measured at various etching times in the initial potential rise in the etching transient, and also during steady-state tunnel growth. According to Eqs. (4.19) and (4.26), the measured potential in this case is given by

$$E = E^{o}_{Al/AlCl_3} + \frac{\delta}{B_f}\ln\left(\frac{i_{C0}}{i_{f0}}\right) + i_{C0}R_S \tag{4.27}$$

Thus from the above expression, it can be understood that during the relatively slow potential rise in the initial stages of etching, the salt film is in a quasi-steady state and responds to such slow variations by changing its thickness δ. The process of repassivation can be explained by using the above expression. When the potential is decreased, the thickness of the salt film reduces by dissolution of chloride ions at the salt-film/solution interface and finally at the repassivation potential the metal surface is covered with a monolayer of adsorbed chloride ions. When the potential is decreased beyond this repassivation potential, the chloride ions desorb from the surface exposing the bare metal surface to the water in the solution, which immediately induces passivation.

When the experimental time scale is short after sudden potential changes, η and ϕ adjust immediately at constant film thickness, but still satisfy the current continuity condition expressed by Eq. (4.25) and the expression for the measured potential given by Eq. (4.26). If we denote the total potential drop across the salt film and the salt-film/solution interface as V, then V = $\eta+\phi$. Thus according to Eq. (4.25), the expression for the dissolution current density becomes,

$$i = i_{L0}\left[\exp\left(b_L^{+}(V-\phi)\right)-\exp\left(-b_L^{-}(V-\phi)\right)\right]+i_{C0}\exp\left(b_C(V-\phi)\right) \tag{4.28}$$

The high-field conduction rate law given by Eq. (4.19) can be rearranged to obtain an expression for the potential drop,

$$\phi = \frac{\delta}{B}\ln\left(\frac{i}{i_{f0}}\right) \tag{4.29}$$

This can be used to eliminate ϕ in Eq. 4.28 to obtain the final expression,

$$i = i_{L0}\left[\left(\frac{i}{i_{a0}}\right)^{-\gamma_L^+}\exp\left(b_L^+V\right)-\left(\frac{i}{i_{a0}}\right)^{\gamma_L^-}\exp\left(-b_L^-V\right)\right]+i_{C0}\exp\left(b_CV\right)\left(\frac{i}{i_{a0}}\right)^{-\gamma_C} \tag{4.30}$$

where $\gamma_L^+ = \frac{b_L^+\delta}{B}, \gamma_L^- = \frac{b_L^-\delta}{B}$ *and* $\gamma_C = \frac{b_C\delta}{B}$. When the conductivity of the film is high, B is large enough so that the values of all the dimensionless groups γ_L^+, γ_L^- and γ_C become less than 10^{-3}. In this case, the corresponding factors can be set to one, and the equation reduces to,

$$i = i_{L0}\left[\exp\left(b_L^+(V)\right)-\exp\left(-b_L^-(V)\right)\right]+i_{C0}\exp\left(b_C(V)\right) \tag{4.31}$$

If b_C is relatively small compared to b_L^+, Eq. (4.31) is consistent with Eq. (4.18) used to fit the current potential data obtained during the dissolution rate measurements.

4.3. Mathematical Model for Pit Initiation during the Early Stages of Etching

In this section, all the electrochemical processes characterized during the initial stages of etching are incorporated into a model. The model is validated by its ability to predict the experimental potential transients obtained for different etching conditions and also the pit size distributions from Scanning Electron Microscopy (SEM). This model is based on the interfacial void hypothesis discussed in the literature review .

4.3.1. Model equations

The current balance equation defines the applied current as the overall contribution from capacitive current, current due to the uniform corrosion processes and the pit dissolution current, as described already in Eq. (4.12)

$$i_{app} = C\frac{dE}{dt} + i_{an} + i_{pit} \tag{4.32}$$

In evaluating the pitting current during dissolution rate measurements, the following expression was used previously.

$$i_{pit} = 2\pi\langle r^2\rangle i_d n_{pit} \tag{4.33}$$

wherein the value of mean square pit depth $\langle r^2\rangle$ was calculated using the SEM results. For the present model it was assumed that all the pits were hemispherical and nucleated with the same initial radius r_o. An etch pit that nucleates at time τ will grow to time t at a constant dissolution velocity V_d. The depth of the etch pit at time t can be given by,

$$r = r_o + V_d(t-\tau) \tag{4.34}$$

If we consider all the etch pits that nucleate during the etching time and their growth, then the pitting current can be expressed as,

$$i_{pit} = 2\pi r_o^2 i_d \int_0^t \left[1 + \frac{V_d}{r_o}(t-\tau)\right]^2 \left(\frac{dN_{pit}}{dt}\right) d\tau \tag{4.35}$$

consistent with the form given in Eq. (4.33). In the above equation, $\frac{dN_{pit}}{dt}$ represents the pit nucleation rate at time τ. High field conduction kinetics, described by Eq. (4.5), was used to express the conduction current density through the oxide film i_{an}. Eq. (4.10) was used to determine the rate of oxide film growth.

Since i_{an} represents the current due to the uniform corrosion processes, the velocity of the metal/film interface V_{mf} can be expressed as,

$$V_{mf} = \frac{i_{an}}{3FC_{Al}} \tag{4.36}$$

where C_{Al} represents the concentration of Al atoms in the metal and F stands for Faraday's constant. According to the uniform void hypothesis, when this interface contacts a void, the oxide film collapses and the pit initiates. Assuming an uniform concentration of voids buried in the metal C_V, the rate of pit nucleation depends directly on the rate at which these voids are exposed. Thus the pit initiation rate $\frac{dN_{pit}}{dt}$ in Eq. (4.35) can be substituted by the following expression,

$$\frac{dN_{pit}}{dt} = \left(\frac{i_{an}}{3FC_{Al}}\right)C_V \tag{4.37}$$

The potentials of interest are much more anodic than the repassivation potential of aluminum, which prevents passivation inside the pit during these early etching times (47, 48). Thus the passivation kinetics for the etch pit is neglected in the model. The numerical code which handles all the above equations to solve for the important parameters i_{an}, i_{pit}, n_{pit} and r is represented by the flow chart shown in Figure 4.19.

4.3.2 Effect of various parameters on the etching behavior of aluminum

Potential transients were measured for different values of some of the important etching parameters. In all of the etching experiments, the sample was immersed in etchant solution for 10 s before actually passing the current. The model was checked for its ability to predict these potential transients. The effect of each parameter, along with the simulation results, is discussed in the following sections.

4.3.2.1 Effect of sodium hydroxide pretreatment time

Potential transients in 1M HCl/3M H_2SO_4 at 70°C and 0.2 A/cm^2 for different pretreatment times in sodium hydroxide are shown as solid lines in Fig 4.20. Since the potential drops down from the maximum once pitting becomes dominant, it was suggested by Martin and Hebert (46) that the time elapsed by the potential peak is inversely proportional to the rate of pit initiation. It can be deduced from the figure that the pit initiation rate initially increases with the pretreatment time and later shows a decreasing trend for times exceeding one minute. Using PAS studies, it was previously observed that the concentration of interfacial voids increased until a pretreatment time of 1 minute in NaOH and later decreased

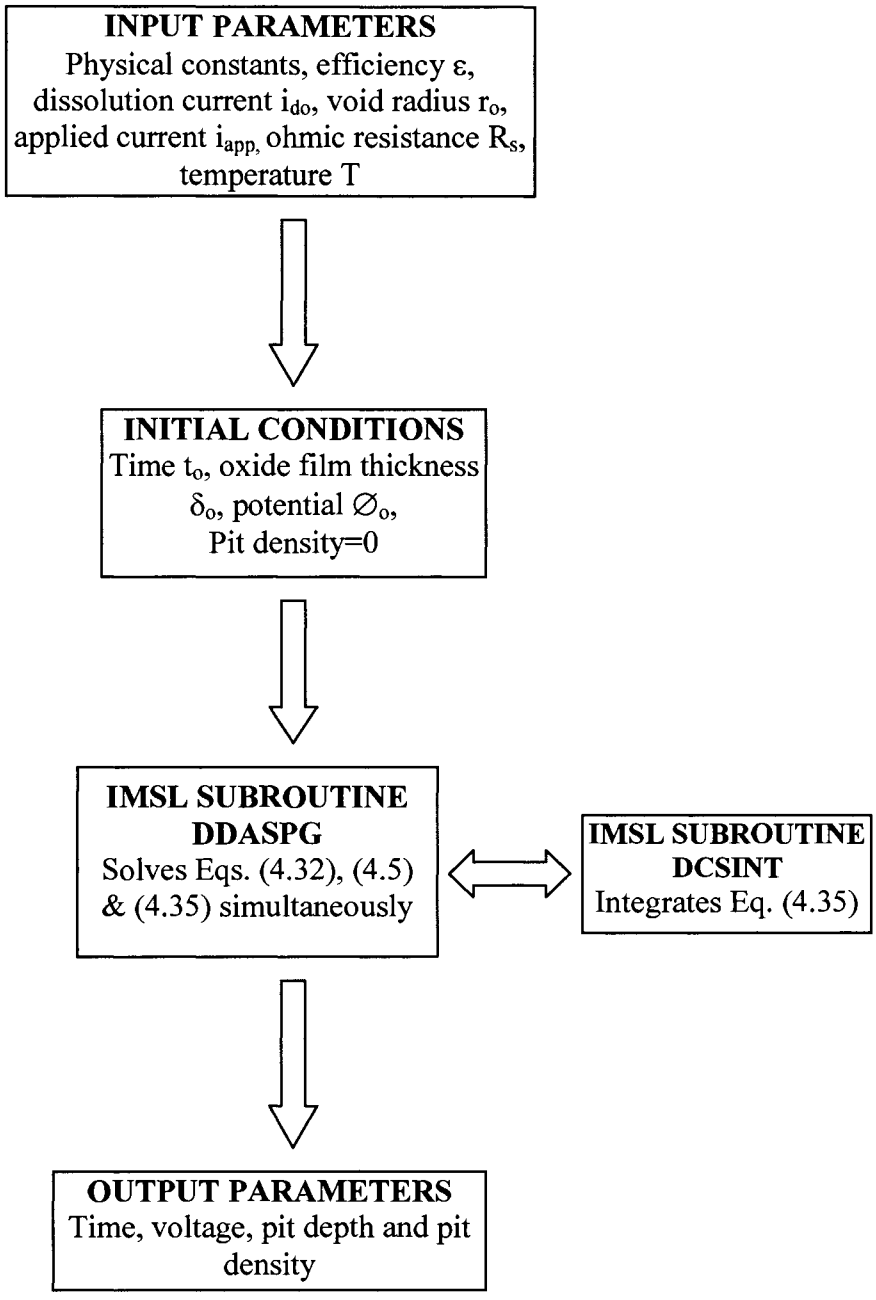

Figure 4.19 Flow chart for the numerical code used for the simulations

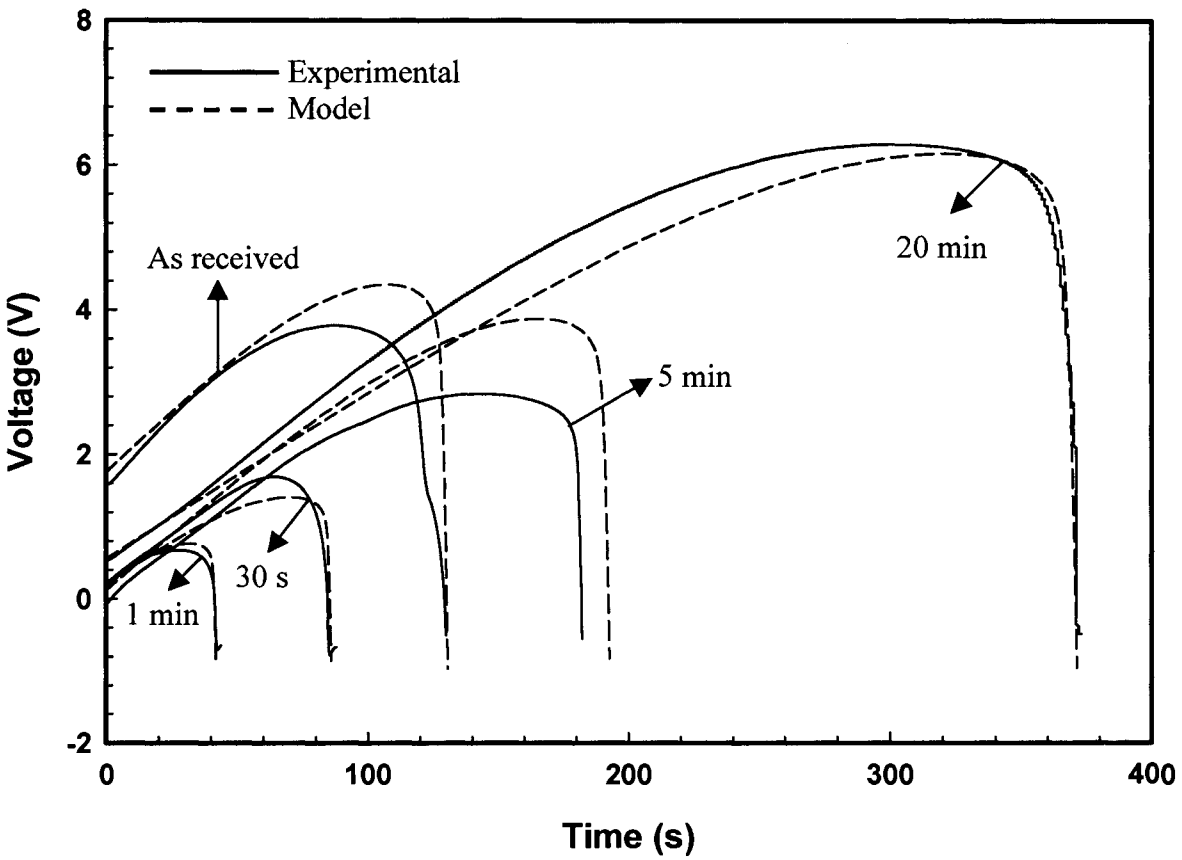

Figure 4.20 Experimental and model transients for different pretreatment times in NaOH. Etching current density 200 mA/cm^2, etchant temperature 70 °C, open circuit (O.C) immersion time 10 s.

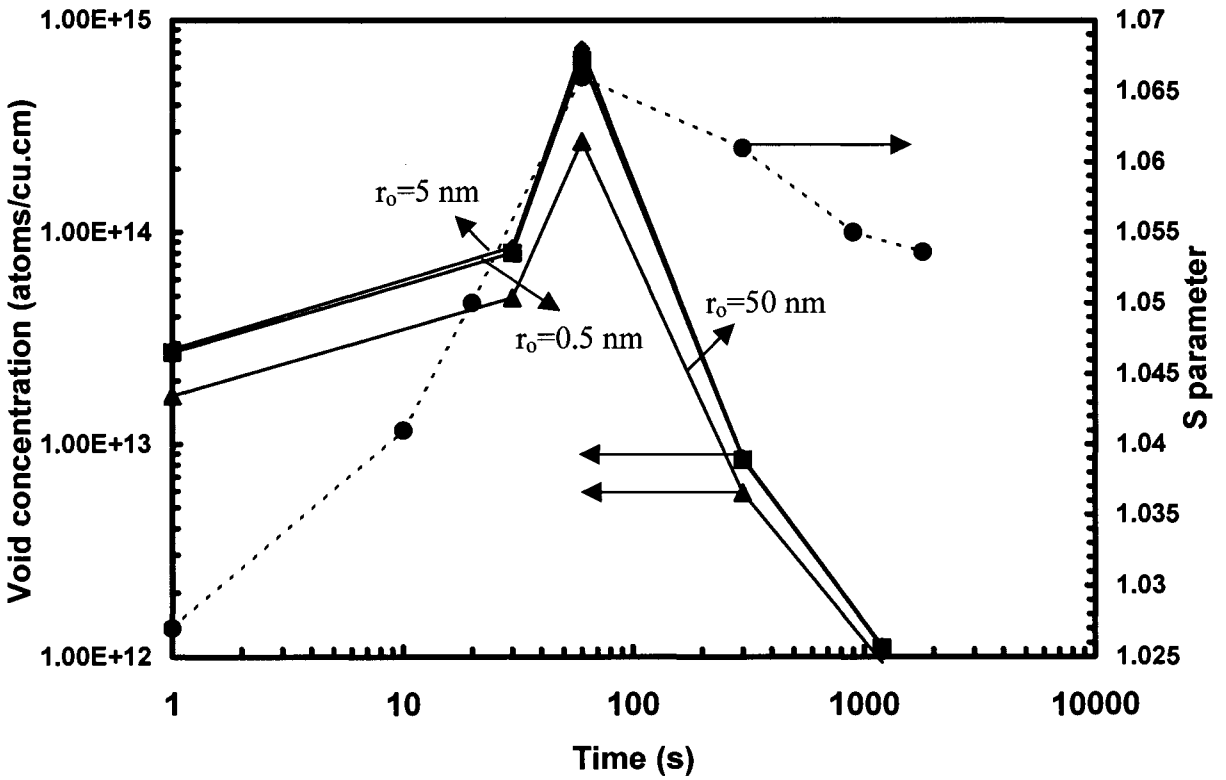

Figure 4.21 Comparison of void concentrations evaluated from PAS results with those fitted using the model.

(41). Wu explained that at prolonged pretreatment times, the rate of void formation is relatively smaller than the rate of at which they are lost due to metal dissolution. Since these interfacial voids are considered to be the pit precursor sites by the hypothesis used, the pit initiation rates are expected to follow the same trend exhibited by the rate of void formation, consistent with the trend exhibited by the potential transients.

In order to simulate the potential transients using the model developed, the values of the initial film thickness evaluated using Eq. (4.5) and the efficiency of oxide film growth evaluated using Eq. (4.11) were fit from parallel experiments done in H_2SO_4 solution. Since the efficiency changes with the instantaneous slope of the potential transient, an average value, for the region where the transients in HCl/H_2SO_4 and H_2SO_4 are coincident, was used in the simulation. The void radius was set to 50 nm which was the minimum pit size observed by SEM after etching the sample for a few ms. The value of r_o which is considered to be the initial radius of the etch pit may actually include the pit growth due to the initial burst of dissolution when the reactive void surface is exposed , since subsurface voids of 100 nm in diameter may be implausible. Based on the dissolution kinetics discussed in Section 4.2, the dissolution current density was taken to be that measured in etch tunnels at the same temperature (61).

The potential transients shown as dotted lines in Figure 4.20 were simulated by fitting C_V to the experimental transients. The figure shows very good agreement between the experimental transients and simulated ones. The fit values of C_V for various values of r_o are compared with the defect layer S parameter values from PAS (41) in Figure 4.21. It can be seen that independent of r_o, both the S parameter and C_V have the same dependence on pretreatment time. This trend is expected, because the S parameter is supposed to scale with

the volume fraction of the voids in the defect layer and therefore with C_V. The final constant potential is not predicted by the model, since passivation kinetics inside the pit are not included in it. The values of high-field conduction kinetic parameters i_{ao} and B were 1.798 x 10^{-12} A/cm^2 and 2.99 cm/MV respectively evaluated from Eq. (4.6). The following table shows the values of various initial parameters used to simulate the model transient.

Table 4.4. Initial and fit values of parameters used in the model

Pretreatment time (s)	**Efficiency**	**Initial thickness (nm)**	**C_V (x 10^{13} atoms/cm^3)**
0	0.29	3.61	1.7
30	0.26	1.77	4.9
60	0.29	1.8	27
300	0.32	1.69	0.59
1200	0.24	2.2	0.094

4.3.2.2. Effect of the applied current density

The potential transients for different etching current densities in 1M HCl/3M H_2SO_4 at 70°C are shown in Figure 4.22, all for 30 s pretreatment time. The time elapsed by the potential peak, t_{pit}, is constant for all the transients indicating that the pit nucleation rate is independent of the applied current density. To simulate the model transients, the C_V value corresponding to 30 s pretreatment was used (Table 4.4). All other parameters were also fixed. It can be seen that the model transients shown as dotted lines are in good agreement

with the experimental ones, with t_{pit} remaining constant in both cases. This behavior can be explained using the model equations. Using Figure 4.1, it was already explained that for most of the etching time elapsed by the potential peak, uniform corrosion processes are dominant. Thus, the approximation can be used that until the time t_{pit}, all of the applied current is supplied by uniform corrosion. It was also explained that when the pitting current completely dominates other current sources, the potential drops abruptly to the steady state value. Thus at t_{pit}, i_{pit} supplies the entire applied current. Based on the above arguments it is reasonable to set i_{an} and i_{pit} to i_{app}, in Eqs. (4.35) and (4.37). When Eq. (4.35) is integrated and the above condition is applied, the following expression is obtained at $t = t_{pit}$

$$\frac{V_d t_{pit}}{r_o} = \left(\frac{3}{2\pi C_V r_o^3} + 1 \right)^{\frac{1}{3}} - 1 \tag{4.38}$$

In deriving Eq. (4.38), the dissolution current density i_d was expressed as,

$$i_d = (V_d)(3FC_{Al}) \tag{4.39}$$

Eq. (4.38) clearly reveals that t_{pit} is independent of the applied current density. When it was used to evaluate t_{pit} for the parameter values used in the simulation, the value obtained was 80 ms consistent with the time period elapsed by the potential peaks of the experimental transients. The independence of t_{pit} on applied current density supports the void hypothesis, since this calculation shows that it follows from the proportionality between pit nucleation rate and the uniform corrosion rate.

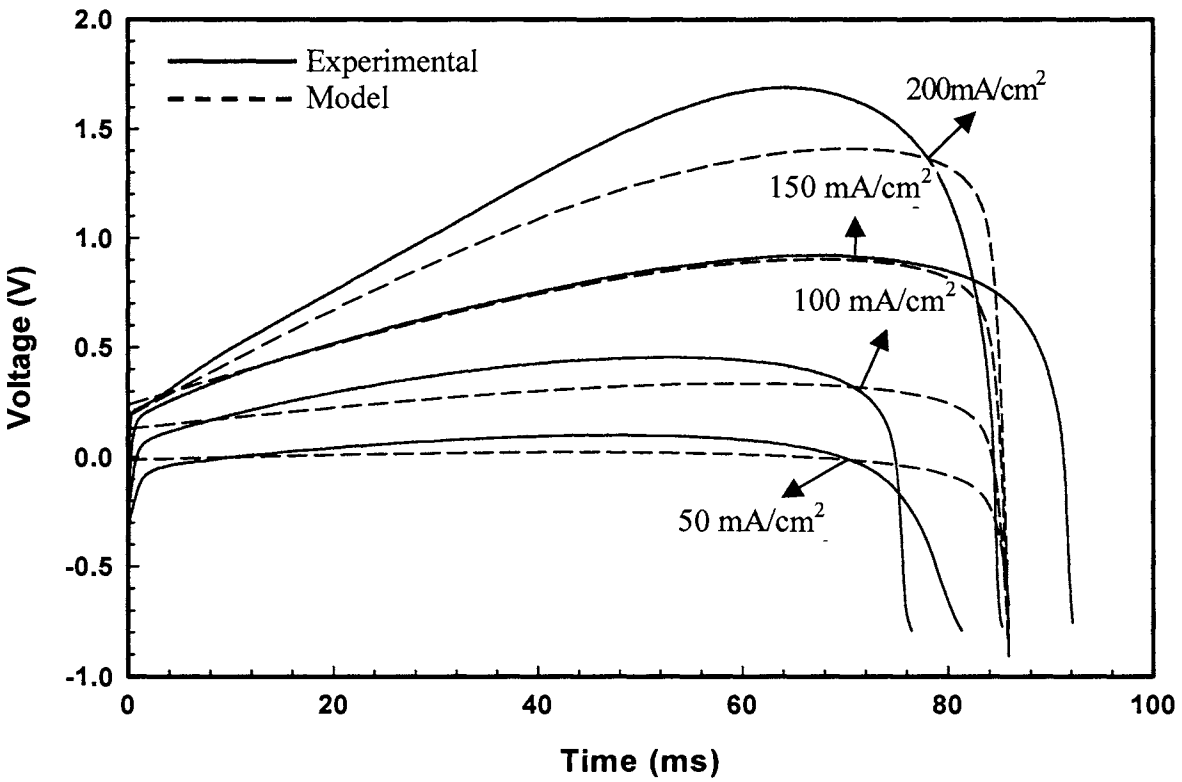

Figure 4.22 Experimental and model transients for different etching current densities. Etchant temperature 70 °C, O.C immersion time 10 s, pretreatment time in NaOH 30 s.

4.3.2.3. Effect of the temperature of the etchant solution

Etching was done for various etchant bath temperatures for a pretreatment time of 30 s and at a current density of 200 mA/cm^2. The corresponding transients are shown in Figure 4.23. It can be seen from the plot that t_{pit} decreases with increasing temperature. In their previous work, Hebert and Alkire showed that the rate of metal dissolution increases with temperature (61). Thus at higher temperatures, pitting becomes dominant at much earlier etching times, consistent with the trend observed in Figure 4.23. The same values of C_V and r_o used to fit the transients corresponding to 30 sec pretreatment time were used here to simulate the model transients. The dissolution velocity V_d was taken from Arrhenius expression found previously (61),

$$V_d = A\exp\left(\frac{-E_a}{RT}\right) \tag{4.40}$$

The values of the pre-exponential factor A and the activation energy E_a were 6.9 x 10^9μm/s and 15 kcal/mol, respectively (61). Figure 4.23 shows that the simulated transients successfully track the trend exhibited by the experimental potential transients. At higher temperatures though, t_{pit} for the model transients is somewhat higher than the experimental ones. The values of t_{pit} predicted by Eq. (4.38) agree well with the simulation values as shown in Table 4.5.

Pit size distributions estimated from SEM images were used to estimate the mean square pit depth at various temperatures. These values were compared to those predicted by the model, as shown in the table. It is clear from the table that, although the predicted r_{rms}

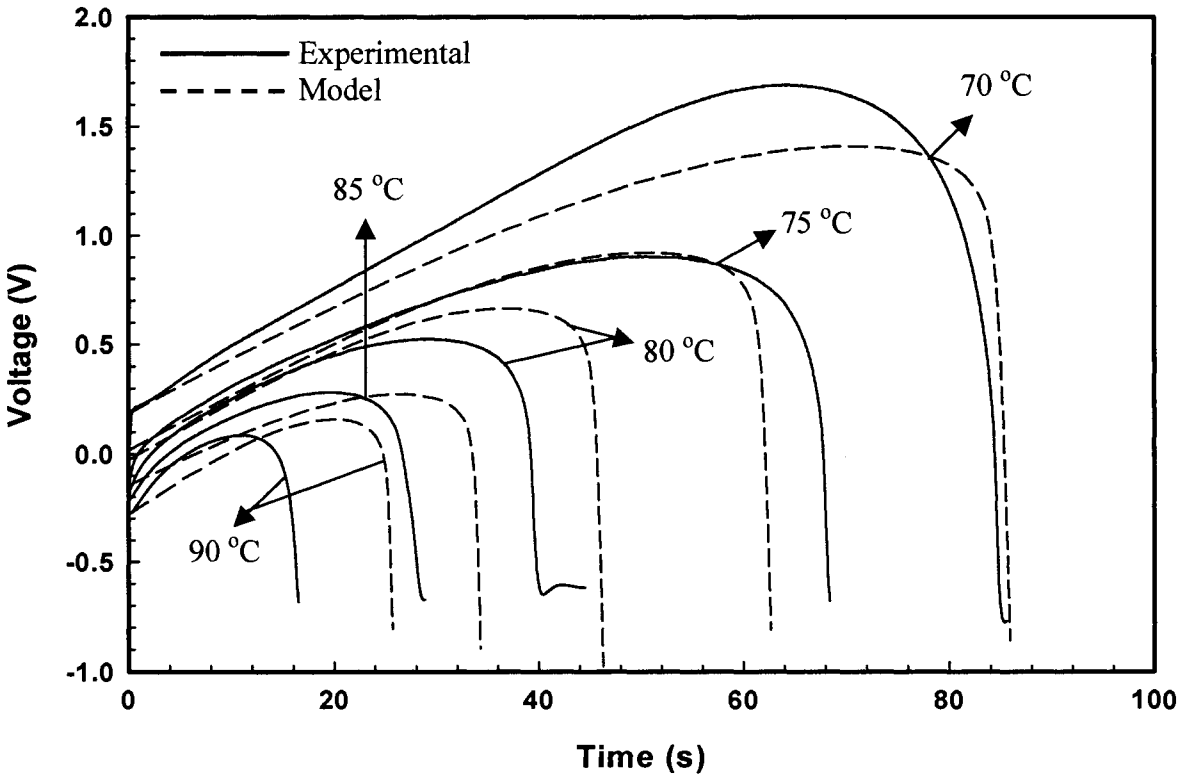

Figure 4.23 Experimental and model transients for different etchant temperatures. Etching current density 200 mA/cm^2, O.C immersion time 10 s and pretreatment time in NaOH 30 s.

Table 4.5. Table showing the experimental and predicted values of t_{pit} and r_{rms}

Temperature (°C)	Experimental t_{pit} (ms)	t_{pit} (ms) by Eq.(4.38)	t_{pit} (ms) by simulation	Experimental r_{rms} (nm)	Predicted r_{rms} (nm)
70	86	79	87	300	162
80	39	52	46	250	159
90	16	19	25	150	160

values do not follow the same trend exhibited by the experimental ones, both of them are comparable. The temperature independence of the simulated r_{rms} values can be explained from the model equations. If the assumption that the uniform corrosion current dominates the applied current till t_{pit} is used, a simplified expression for r_{rms} is obtained,

$$\frac{r_{rms}^2}{r_0^2} = \frac{r_0}{3V_d t_{pit}}\left[\left(1+\frac{V_d t_{pit}}{r_0}\right)^3 - 1\right] \tag{4.41}$$

which is independent of temperature. The value of r_{rms} from Eq. (4.41), agrees with the predicted values shown in Table 4.5. The temperature dependence shown by the experimental r_{rms} may be due to the lack of a uniform void concentration beneath the oxide film. Also, the temperature dependence of the initial burst of the pit growth may play a significant role in the evaluation of r_{rms}.

4.3.2.4. Effect of open circuit immersion time in the etchant

Open circuit (O.C) immersion time refers to the brief period during which the sample is immersed in the etching solution before actually passing the etching current. The

experimental transients shown in Figure 4.24 indicate that the rate of pit initiation increases with the immersion time. This is probably due to the additional formation of voids during the brief immersion time, apart from the pretreatment time. Thus the concentration of voids and hence the pit nucleation rate increases with the immersion time. To simulate the model transients the values for efficiency of oxide growth and the initial thickness of the oxide film were obtained from the parallel experiments in H_2SO_4 solution, r_o was taken to be 50 nm and the C_V values were obtained by fitting the model transients to the experimental ones similar to the procedure followed before. These values are shown in Table 4.6.

Table 4.6. Parameter values used for the simulation

Immersion time (ms)	**Efficiency (%)**	**Oxide film thickness (nm)**	**C_V (x 10^{14} atoms/cm^3)**
10	26	1.77	0.49
15	27	1.67	1.1
18	32	1.67	10
25	40	1.54	26
40	45	1.35	75

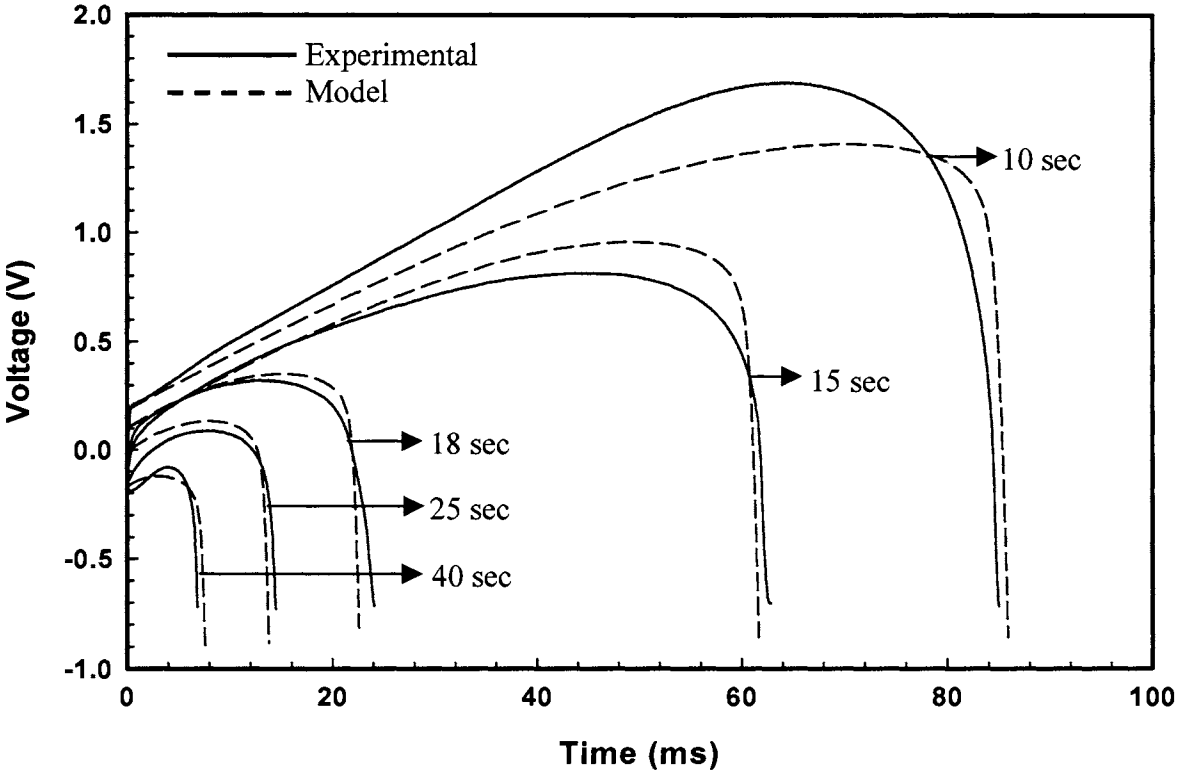

Figure 4.24 Experimental and model transients for different values of O.C immersion time. Etching current density 200 mA/cm^2, etchant temperature 70 °C, pretreatment time in NaOH 30 s .

4.3.2.5. Effect of the chloride ion concentration

Etching was done for various chloride concentrations in the etchant solution at standard etching conditions of 70 °C, 200 mA/cm^2 and 30 s pretreatment time in NaOH. The transients shown in Figure 4.25 indicate that pitting becomes dominant much earlier at elevated chloride concentrations. The SEM images shown in Figure 4.26 reveal increased pit densities at high chloride concentrations. This effect cannot be attributed to NaOH pretreatment effect since the images shown are for the same pretreatment time. One explanation is that the rate of void formation during the open circuit immersion time is comparatively higher for etchants with high chloride concentrations. In order to explore this, two foils pretreated for 30 s in NaOH were etched in 1M HCl/3M H_2SO_4 at standard etching conditions. But prior to etching, both the foils were immersed for 10 s in two different etching solutions of varying chloride concentrations, at 70 °C. This enabled us to study the effect of the chloride ion concentration during the brief immersion time before the etching current was applied. The potential transients obtained during etching of these two foils are compared with the transient corresponding to standard etching conditions in Figure 4.27. The figure shows that compared to the standard etching transient, the other two transients corresponding to increased open circuit immersion time have approximately the same values of t_{pit}. This indicates that the rate of void formation during the O.C immersion in these etchants is nearly the same. Thus, there is no significant effect of the variation in chloride concentration during the O.C immersion time.

Another explanation is that the probability of a void becoming a pit during etching is dependent upon the concentration of the chloride ions in the etchant. Higher chloride concentrations may enhance the stability of the adsorbed chloride layer on the exposed void surface. This layer is necessary so that the surface is not passivated by water.

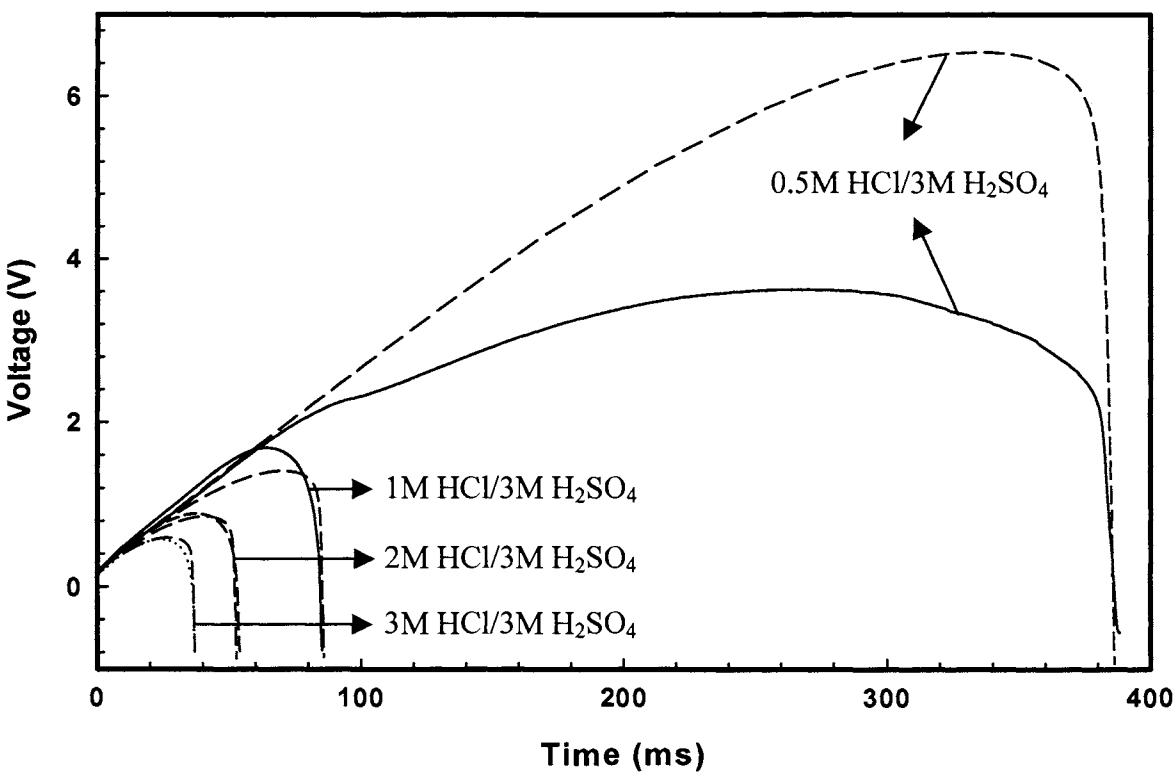

Figure 4.25 Experimental and model transients for etching done using solutions of varying chloride concentrations. Etching current density 200 mA/cm^2, etchant temperature 70 ^{o}C, pretreatment time in NaOH 30 s & O.C immersion time 10 s.

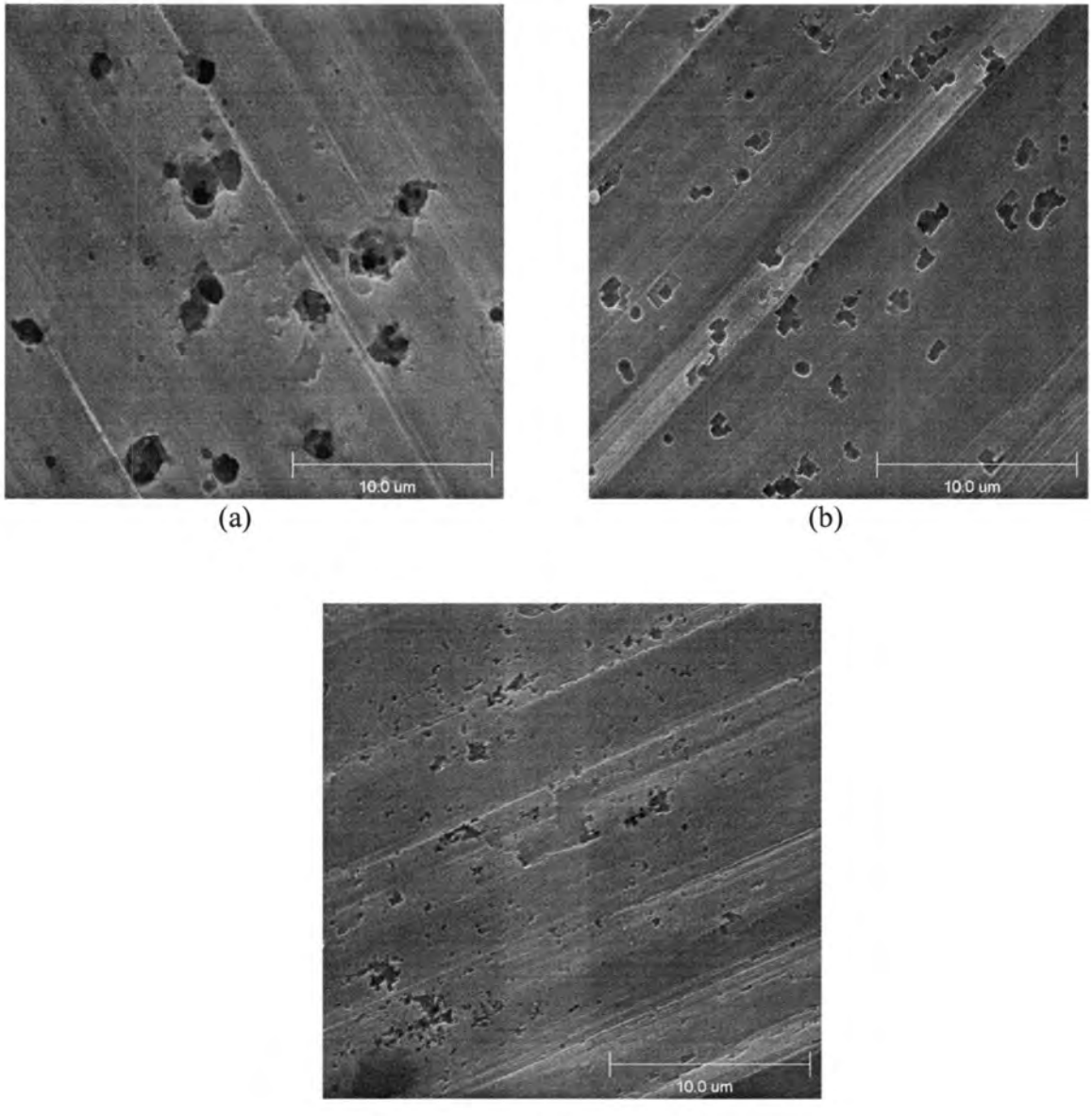

(a) (b)

(c)

Figure 4.26 SEM images for etching done with solutions of varying chloride concentrations magnification 4000x. (a) 0.5M HCl/3M H_2SO_4 (b) 1M HCl/3M H_2SO_4 (c) 3M HCl/3M H_2SO_4. Etching current density 200 mA/cm^2, etchant temperature 70 ^oC, pretreatment time in NaOH 30 s and pretreatment time 10 s.

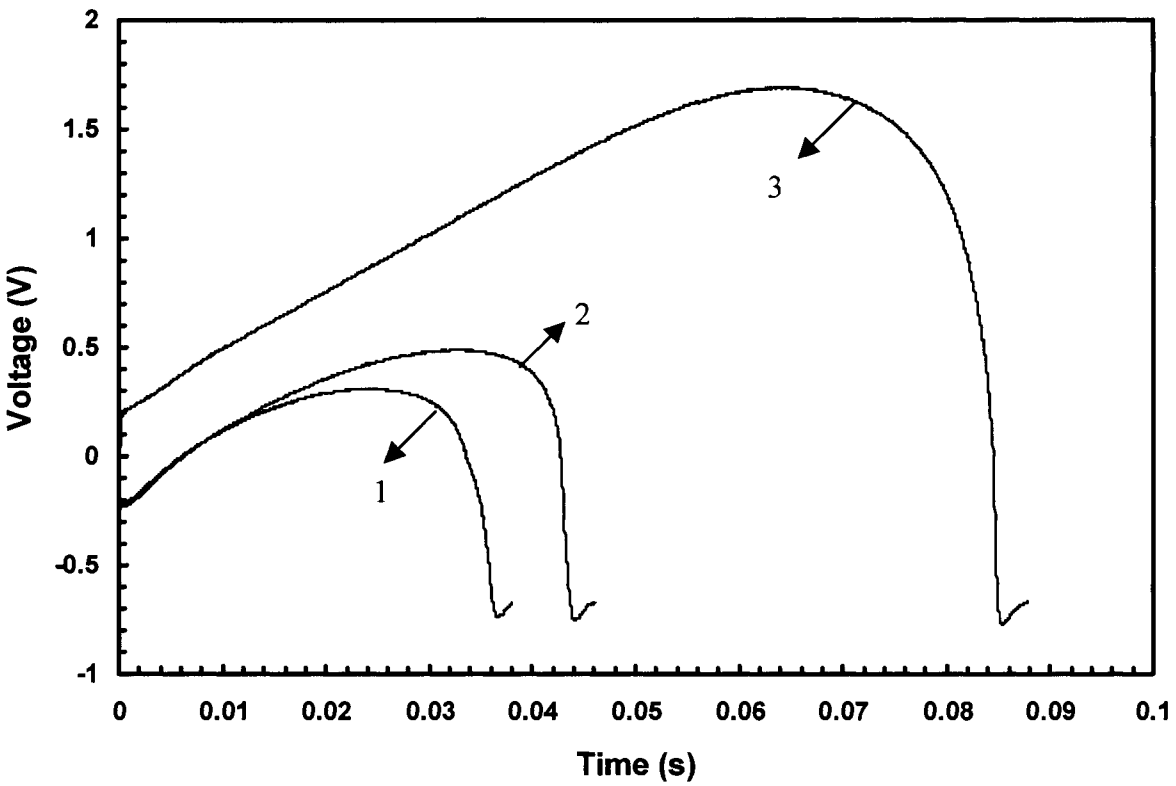

Figure 4.27 Comparison of potential transients for different O.C immersion times at 70 °C in etchants of varying chloride concentrations, after NaOH treatment. Etching current density 200 mA/cm^2, etchant temperature 70 °C, pretreatment time in NaOH 30 s. (1) 10 s in 3M H_2SO_4/3M HCl + 10 s in 3M H_2SO_4/1M HCl (2) 20 s in 3M H_2SO_4/1M HCl (3) 10 s in 3M H_2SO_4/1M HCl

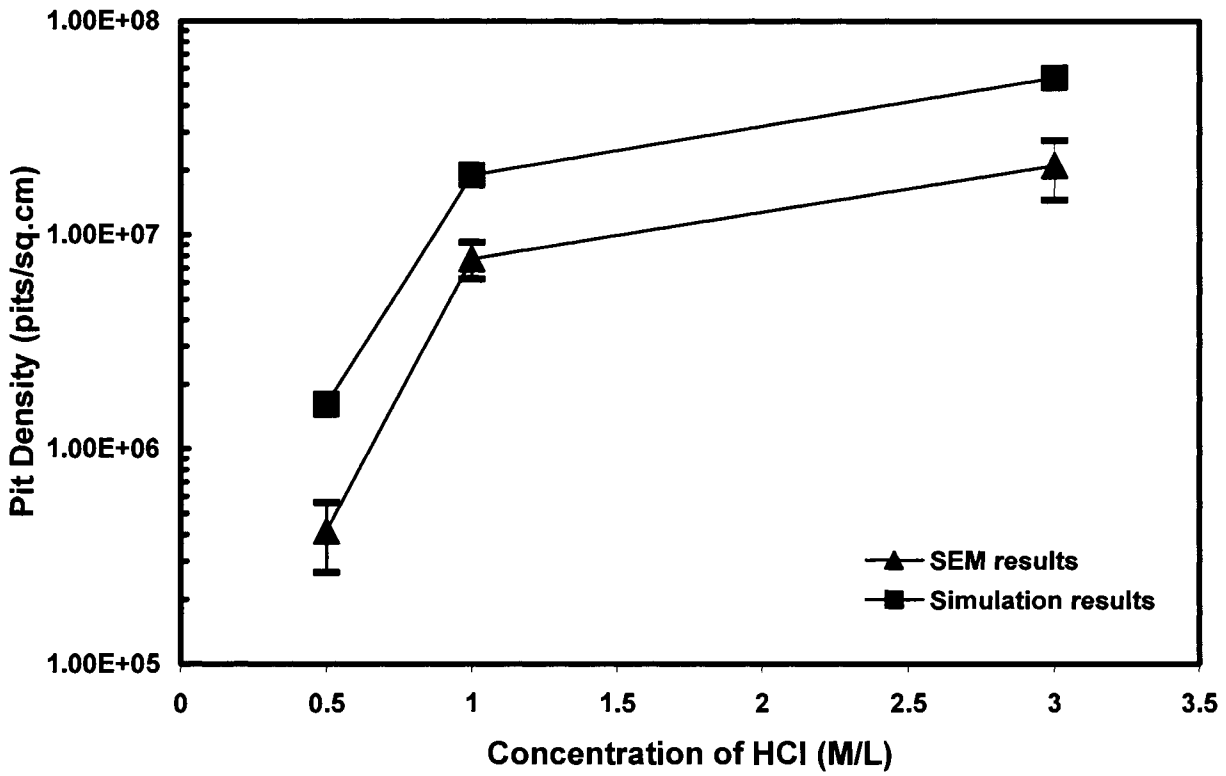

Figure 4.28 Comparison of pit densities predicted by model and evaluated from SEM results for etchants of varying chloride concentrations and etching done at applied current density 200 mA/cm^2, etchant temperature 70 ^{o}C, pretreatment time NaOH 30 s and O.C immersion time 10 s.

In case of solutions with low chloride concentrations, some of the oxygen atoms from water molecules may also get adsorbed on the metallic surface of the void inducing passivation so that the void becomes inactive pit.

The model transients shown in Figure 4.25 were obtained by fitting the C_V values to the experimental transients. As explained earlier, these C_V values represent the net concentration of voids that are effectively transformed into active etch pits. Pit densities predicted by the model for various chloride concentrations are compared to those evaluated from SEM images, in Figure 4.28. Although both of them follow the same trend, the model values are an order of magnitude higher than the experimental values. A more detailed study on the role of chloride ion kinetics in the pit initiation mechanism, might lead to better model predictions.

4.3.2.6. Effect of stirring the etching solution

As-received foils were etched at standard conditions with and without stirring the etchant. The corresponding potential transients are shown in Figure 4.29. The transients indicate that the rate of pit initiation is relatively high when the etchant is stirred. This kind of behavior might be due to the concentration of voids being increased during open circuit immersion in case of stirring. To explore this possibility, an experiment was carried out in which an as-received sample was immersed in unstirred etchant for the standard open circuit immersion time of 10 s, but stirring was initiated when etching began. This potential transient is compared to the standard etching transient in Figure 4.29.

Large difference in t_{pit} can be observed between these two transients. But when the above transient was compared to the one wherein the etchant was kept unstirred during both

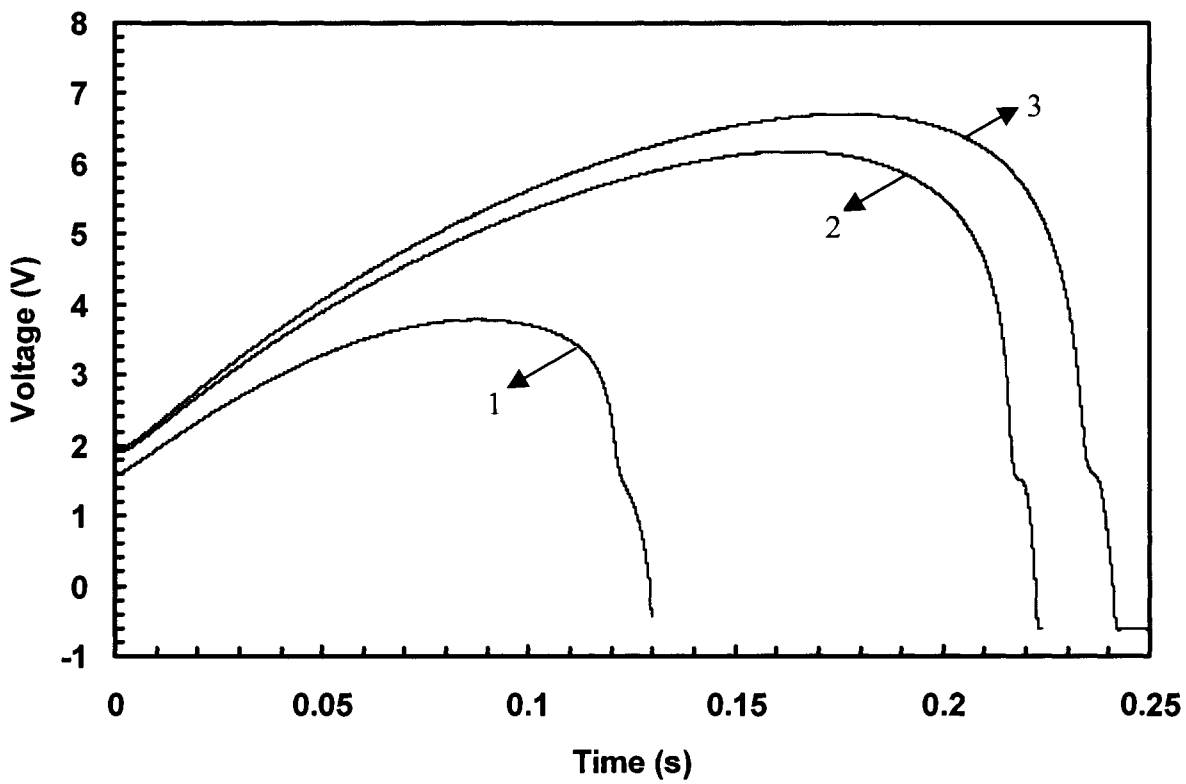

Figure 4.29 Potential transients for as-received foil etched with and without stirring. Etching current density 200 mA/cm^2, etchant temperature 70 ^{o}C and pretreatment time in NaOH 30 s (1) O.C immersion and etching with stirring (2) O.C immersion without stirring and etching with stirring (3) O.C immersion and etching without stirring

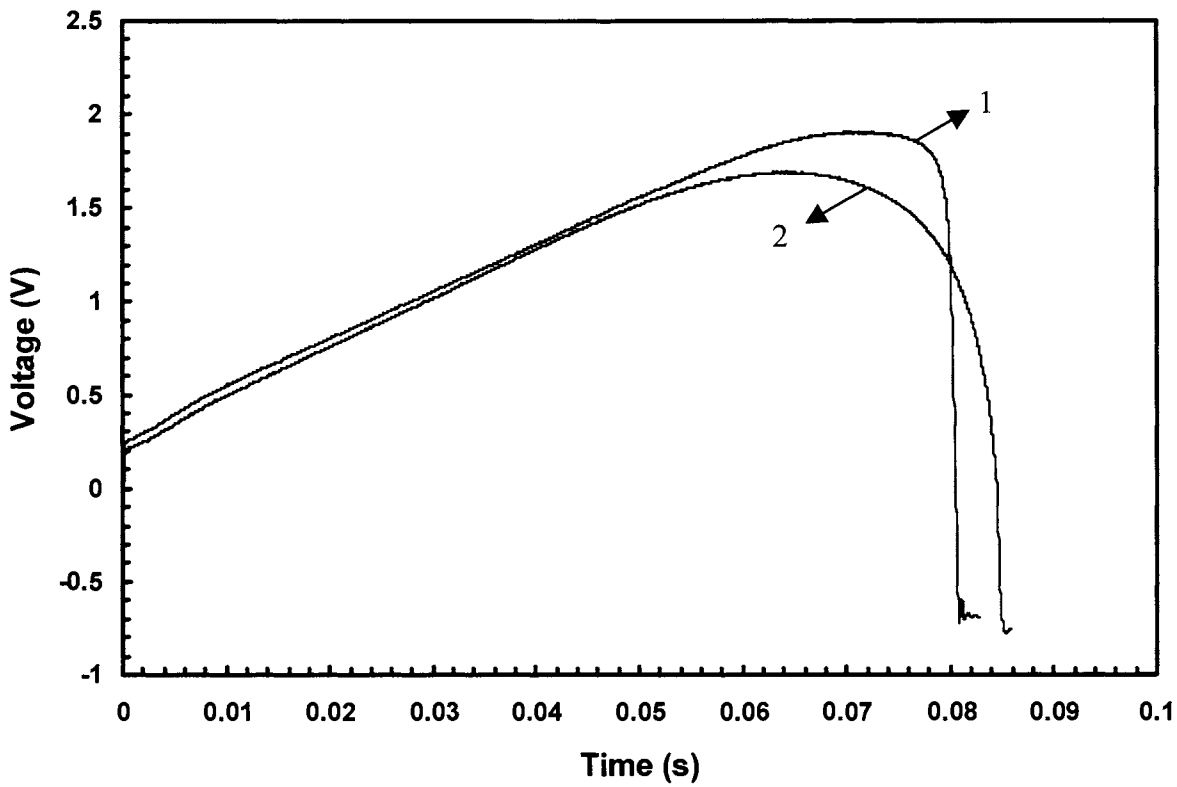

Figure 4.30 Potential transients for 30 s pretreated foil etched with and without stirring. Etching current density 200 mA/cm^2, etchant temperature 70 ^{o}C

(1) O.C immersion and etching without stirring (2) O.C immersion and etching with stirring.

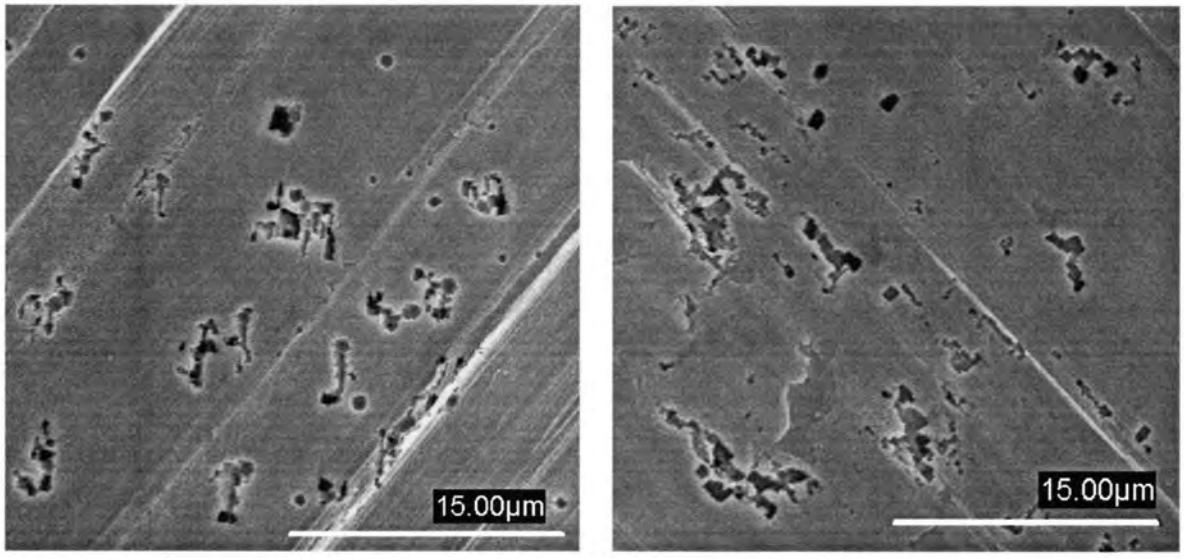

(a) (b)

Figure 4.31 SEM images of 30 s pretreated foils. Etching current density 200 mA/cm^2, etchant temperature 70 ^{o}C. (a) O.C immersion and etching with stirring (b) O.C immersion and etching without stirring.

open circuit immersion and etching, a similar t_{pit} was found. This suggests that the effect of stirring plays a role only during the open circuit immersion time, which ultimately alters the etching behavior.

The effect of stirring during etching of pretreated foils is shown in Fig 4.30. The two transients which correspond to 30 s pretreatment in NaOH have almost the same t_{pit} indicating that the stirring effects are negligible for pretreated foils. Also the SEM images of pretreated foils, etched with and without stirring, in Figure 4.31 reveal similar pit densities. The possible reason for this behavior is that the concentration of voids created during the pretreatment time is so high that it nullifies the effect of stirring during the open circuit immersion.

5. CONCLUSION

Electrochemical processes during the very early stages of etching were thoroughly characterized using various experimental techniques, in order to determine the influence of the voids on pit nucleation. It is found that pitting becomes dominant only after a brief incubation period, which is dominated by the uniform corrosion processes such as uniform metal dissolution and oxide growth.

In exploring the mechanism of metal dissolution, time dependent dissolution kinetics was observed. To explain this phenomenon, the presence of an aluminum chloride salt layer over the active surface of the pit was hypothesized and Vetter-Gorn kinetics were applied to develop a kinetic model. The model was validated by its ability to predict the constant and potential dependent dissolution rates consistent with the measured dissolution rates through current step experiments. If the conduction kinetics of the salt film is known, the model can further be validated by testing the basic assumptions in deriving the final expression of dissolution kinetics given by Eq. (4.31). The present dissolution rate measurements extended to very high current densities on the order of 1000 A/cm^2 and the measurements of time scale dependent dissolution kinetics are quite unusual. Thus a kinetic model that qualitatively agrees with this behavior of dissolution kinetics is noteworthy.

The process of pit initiation during the initial moments of constant-current anodic etching of aluminum in HCl-H_2SO_4 solutions was simulated using a mathematical model. The model incorporated all of the electrochemical processes characterized and was based on the interfacial void hypothesis according to which the subsurface voids are the primary pit initiation sites. Experiments varied the values of primary etching parameters like

pretreatment time, applied current density, temperature of etchant and open circuit immersion time in etchant. The model predictions were in good agreement with the experimental ones, thus validating both the model and the interfacial void hypothesis. But in one case, the model could not predict the experimental findings that pit depths decreased with increasing temperature. The initial burst in pit growth during pit nucleation being neglected in the model, might be one of the reasons for this disagreement.

The effects of chloride ion concentration and stirring were studied by analyzing the corresponding potential transients. To simulate the ideal model transients corresponding to the experiments for various chloride concentrations, the role of chloride ions in pit initiation and growth should be studied in detail and those kinetics should be incorporated into the present model. PAS studies on the variation of void concentration for various open circuit immersion times and for different rates of stirring starting from no stirring condition to very high rates of stirring, could be a better way to substantiate the argument that the concentration of voids increases with open circuit immersion time and stirring. Also, the same samples could be etched and subjected to SEM observations, to explore the effect of these two parameters on the pit initiation rates.

BIBLIOGRAPHY

1) X. Wu, P. Asoka-Kumar, K. G. Lynn and K. R. Hebert, *J. Electrochem. Soc.*, **141**, 3361 (1994).

2) Y. Tak, N. Sinha and K. R. Hebert, *J. Electrochem. Soc.*, **147**, 4103 (2000).

3) K. J. Vetter and F. Gorn, *Electrochim. Acta*, **18**, 321 (1973).

4) R. Kirchheim, *Electrochim. Acta*, **32**, 1619 (1987).

5) H.-H. Strehblow, *Werk. Korros.*, **27**, 792 (1976).

6) T. P. Hoar, D. C. Mears and G. P. Rothwell, *Corros. Sci.*, **5**, 279 (1965).

7) J. B. Bessone, D. R. Salinas, C. E. Mayer, M. Ebert and W. J. Lorenz, *Electrochim. Acta*, **37**, 2283 (1992).

8) C. L. McBee and J. Kruger, in "Localized Corrosion", R. W. Staehle et al., Editors, p.252, NACE, HOUSTON, (1974).

9) H. H. Uhlig, *J. Electrochem. Soc.*, **97**, 215C (1950).

10) H. Bohni and H. H. Uhlig, *J. Electrochem. Soc.*, **116**, 906 (1969).

11) H. P. Leckie and H. H. Uhlig, *J. Electrochem. Soc.*, **113**, 1262 (1966).

12) Y. M. Kolotyrkin, *J. Electrochem. Soc.*, **108**, 209 (1961).

13) T. P. Hoar, *Disc. Faraday Soc.*, **No.1**, 299 (1947).

14) T. P. Hoar, *Trans. Faraday Soc.*, **45**, 683 (1949).

15) J. A. Richardson and G. C. Wood, *Corros. Sci.*, **10**, 313 (1970).

16) N. Sato, *Electrochim. Acta*, **16**, 1683 (1971).

17) T. P. Hoar, *Corros. Sci* . **7**, 355 (1967).

18) T. P. Hoar and W. R. Jacob, *Nature*, **216**, 1299 (1967).

19) Z. A. Foroulis and M. J. Thubrikar, *J. Electrochem. Soc.*, **122**, 1296 (1975).

20) T. P. Hoar, *Trans. Faraday Soc.*, **33**, 152 (1937).

21) J. R. Galvele, *J. Electrochem. Soc.*, **123**, 464 (1976).

22) J. R. Galvele, J. B. Lumsden and R. W. Staehle, *J. Electrochem. Soc.*, **125**, 1204 (1978).

23) Z. Szklarska-Smialowska, Pitting Corrosion of Metals, National Association of Corrosion Engineers, Houston, Texas, (1986).

24) G. S. Eklund, *J. Electrochem. Soc.*, **121**, 467 (1974).

25) G. Wranglen, *Corros. Sci.*, **14**, 331 (1973).

26) R. M. Rynders, C.-H. Paik, R. Ke and R. C. Alkire, *J. Electrochem. Soc.*, **141**, 1439 (1994).

27) K. Nisancioglu, K. Y. Davanger and O. Strandmyr, *J. Electrochem. Soc.*, **128**, 1523 (1981).

28) K. Kowal, J. DeLuccia, J. Y. Josefowicz, C. Laird and G. C. Farrington, *J. Electrochem. Soc.*, **143**, 2471 (1996).

29) L. L. Shreir, R. A. Jarman and G. T. Burstein, in Corrosion, Vol. 1, L. L. Shreir, R. A. Jarman, and G. T. Burstein, Editors, Butterworths-Heinemann, Ltd., London (1994).

30) D.E.Williams, C. Westcott and M.Fleischmann, *J. Electrochem. Soc.*, **132**, 1804 (1985).

31) D.E.Williams, C. Westcott and M.Fleischmann, *J. Electrochem. Soc.*, **132**, 1796 (1985).

32) J. Stewart, P. H. Balkwill and D. E. Williams, *Corros. Sci.*, **36**, 1213 (1994).

33) Y. Zhu and D. E. Williams, *J. Electrochem. Soc.*, **144**, L43 (1997).

34) D. E. Williams, J. Stewart and P. H. Balkwill, in Critical Factors in Localized Corrosion, Gerald S. Frankel and Roger C. Newman, Editors, PV 92-9, p.36, The Electrochemical Society Proceedings Series, Pennington, NJ (1992).

35) S. T. Pride, J. R. Scully and J. L. Hudson, *J. Electrochem. Soc.*, **141**, 3028 (1994).

36) C. Y. Chao, L. F. Lin and D. D. MacDonald, *J. Electrochem. Soc.*, **128**, 1187 (1981).

37) L. F. Lin, C. Y. Chao and D. D. MacDonald, *J. Electrochem. Soc.*, **128**, 1194 (1981).

38) A. Alum, H. P. Heighly and R. N. West, *J. Phys. F : Met. Phys.*, **12**, 399 (1982).

39) P. E. Doherty and R. S. Davis, *Acta Metall.*, **7**, 118 (1959).

40) P. E. Doherty and R. S. Davis, *J. Appl. Phys.*, **34**, 619 (1963).

41) K. R. Hebert, H. Wu, T. Gessman and K. G. Lynn, *J. Electrochem. Soc.*, **148**, B92 (2001).

42) X. Wu and K. R. Hebert, *J. Electrochem. Soc.*, **143**, 83 (1996).

43) A. Cigada, G. Rondelli, B. Vicentini and G. Dollaspezia, Proceedings of NACE, Houston, TX, 1993, p. 1938.

44) K. Arai, T. Suzuki and T. Atsumi, *J. Electrochem. Soc.*, **132**, 1667 (1985).

45) R. B. Diegle, *J. Electrochem. Soc.*, **121**, 583 (1974).

46) T. Martin and K. R. Hebert, *J. Electrochem. Soc.*, B101 (2001).

47) B. J. Wiersma and K. R. Hebert, *J. electrochem. Soc.*, **138**, 48 (1991).

48) N. Osawa, K. Fukuoka and z.-i. Tanabe, *Sumitomo Light Met. Tech. Rep.*, **33**, 40 (1992).

49) B. J. Wiersma, Metal Dissolution and Passivation in Etch Pits and Tunnels on Aluminum (Ph. D Thesis), Iowa State University, Ames, IA (1990).

50) J. Flis and L. Kowalczyk, *J. Appl. Electrochem.*, **25**, 501 (1995).

51) N. Osawa and K. Fukuoka, *Corros. Sci.*, **42**, 585 (2000).

52) F. Hunkeler and H. Bohni, Ottawa, in Proceedings of the International Congress on Metallic Corrosion, Vol. 2, p.163, National Research Council Of Canada, Ottawa (1984).

53) F. Hunkeler and H. Bohni, *Corrosion*, **37**, 645 (1981).

54) G. S. Frankel, *Corrosion*, **37**, 645 (1990).

55) G. S. Frankel, J. R. Scully and C. V. Jahnes, *J. Electrochem. Soc.*, **143**, 1834 (1996).

56) T. R. Beck, *Electrochim. Acta.*, **29**, 485 (1984).

57) T. R. Beck and R. C. Alkire, *J. Electrochem. Soc.*, **129**, 1663 (1979).

58) K. P. Wong and R. C. Alkire, *J. Electrochem. Soc.*, **137**, 3010 (1990).

59) D. W. Buzza and R. C. Alkire, *J. Electrochem. Soc.*, **142**, 1104 (1995).

60) R. S. Alwitt, H. Uchi, T. R. Beck and R. C. Alkire, *J. Electrochem. Soc.*, **131**, 13 (1984).

61) K. Hebert and R. Alkire, *J. Electrochem. Soc.*, **135**, 2447 (1988).

62) E. Makino, T. Yajima, T. Shibata, M. Ikeda, Y. Tanno and E. Suganuma, *Mater. Trans., JIM*, **34**, 796 (1993).

63) C. F. Lin and K. R. Hebert, *J. Electrochem. Soc.*, **137**, 3723 (1990).

64) Z. Ashitaka, G. E. Thompson, P. Skeldon, G. C. Wood, H. Habazaki and K. Shimizu, 132 (2000). *J. Electrochem. Soc.*, **147**, 132 (2000).

65) A. Despic and V. P. Parkhutik, in J. O'M. Bockris, R. E. White and B. E. Conway, Editors, Vol. 20, p. 401 (1989).

66) B. J. Wiersma, Y. Tak and K. R. Hebert, *J. Electrochem. Soc.*, **138**, 371 (1991).

67) A. C. Harkness and L. Young, *Can. J. Chem.*, **44**, 2409 (1966).

68) M. Pourbaix, "Atlas of Electrochemical Equilibria in Aqueous Solutions," Pergamon Press, New York (1966).

69) NIST-JANAF Thermochemical Tables, Fourth Edition, Part I, M. W. Chase, Editor, p. 156, American Institute of Physics and American Chemical Society, Woodbury, New York (1998).

70) Y. Tak, N. Sinha and K. R. Hebert, *J. Appl. Electrochem.*, **147**, 4103 (2000).

71) K. R. Hebert, Studies on the Control of Metal Passivation in the Electrochemical Tunnel Etching of Aluminum (Ph. D Thesis), University of Illinois, Urbana-Champaign, IL (1985).

ACKNOWLEDGEMENTS

First of all, I would like to extend my sincere thanks to my advisor Dr. Kurt R. Hebert for his constant support and encouragement throughout my stay in ISU. I am pretty sure that without his guidance, this work would not have seen the light of the day. His major input for the kinetic model and the simulation helped me to complete this work in a timely manner. When it came to personal matters, his support and care had always given me comfort and motivation. In this regard, I have no words to express my sincere thanks to him.

I am grateful to Dr. Thomas Strange (St. Jude Medical Inc.) for funding this work. My sincere thanks are due to Dr. Charles Glatz for supporting me financially by extending the funding after my defense. I would like to thank Mr. Takeshi Makino for his helpful discussions regarding the etching experiments. I would like to thank my POS committee members, Dr. Rodney O. Fox and Dr. Vikram L. Dalal for their co-operation. My sincere thanks are due to Dr. L. K. Doraiswamy for his motivation and care.

I would like to thank Mr. Jerry Amenson and Mr. Warren Straszeim for teaching me the techniques of Scanning Electron Microscope and allowing me to use it.

Next, I would like to thank my group members for the lively moments we shared during research discussions and particularly Renchun and Huiquan for introducing me to Atomic Force Microscopy.

My heartiest thanks to my parents, sister, brother-in-law and my uncle for their constant love and encouragement from miles away. I consider myself very lucky for having the support from my close friends here at ISU and particularly Vivek, Murali, and Anil for their valuable suggestions in my final preparations.

I also take this opportunity to extend my heartiest thanks to my professors back in India, Dr. N. G. Renganathan and Dr. S. Mohan and my seniors Venkat and Sudershan. Without their help and support, I could not have stepped into ISU. My thanks are due to all those who directly or indirectly helped me on various fronts during my research.